Acta Materialia 301 (2025) 121531

Contents lists available at ScienceDirect

Acta Materialia

journal homepage: www.elsevier.com/locate/actamat

Full length article

Ordering by ultrasonic excitation for achieving an excellent catalytic performance of metallic glasses

Wei Li [a,1], Jiayi Ruan [a,1], Zhenghao Gu [a], Luyao Li [a,b], Hua Yang [c], Yubin Ke [c], Xuelian Wu [d], Yujiao Lu [e], Zheng Wang [e], Fujun Lan [f,g,h], Qiaoshi Zeng [f,g], Jiang Ma [b], Xun-Li Wang [i], Chenchen Yuan [a,*]

[a] School of Materials Science and Engineering, Jiangsu Key Laboratory for Advanced Metallic Materials, Southeast University, Nanjing 211189, China
[b] Shenzhen Key Laboratory of High Performance Nontraditional Manufacturing, College of Mechatronics and Control Engineering, Shenzhen University, Shenzhen, 518060, China
[c] China Spallation Neutron Source, Dongguan Branch, Institute of High Energy Physics, Chinese Academy of Sciences, Dongguan, 523803, China
[d] Advanced Ceramics Research Center, School of Materials Science and Engineering, Anhui University of Technology, 243032, Ma'anshan, China
[e] Key Laboratory for Liquid–Solid Structural Evolution and Processing of Materials (Ministry of Education), Shandong University, Jinan, 250061, China
[f] Center for High Pressure Science and Technology Advanced Research, Shanghai 201203, China
[g] Shanghai Key Laboratory of Material Frontiers Research in Extreme Environments (MFree), Institute for Shanghai Advanced Research in Physical Sciences (SHARPS), Shanghai 201203, China
[h] Shanghai Institute of Laser Plasma, Shanghai 201203, China
[i] Department of Physics and Center for Neutron Scattering, City University of Hong Kong, 83 Tat Chee Avenue, Kowloon, Hong Kong, China

ARTICLE INFO

Keywords:
Metallic glasses
Ultrasonic treatment
Ordering
Degradation

ABSTRACT

Developing novel high-efficiency and low-cost catalysts for environmental wastewater treatment is of great importance for both industrial application and scientific research. Conventional crystalline catalysts face significant challenges, including high production costs, complex synthesis procedures, limited catalytic activity, etc. Herein, the selected $Fe_{76}Cr_2Si_{11}B_{11}$ metallic-glass (MG) powders were mechanically vibrated via ultrasonic treatment (UT) with controllable energy inputs just within ~1 s for achieving highly effective degradation of azo dye wastewater. Remarkably, the UT-optimized MG exhibits exceptional catalytic performance for the complete decolorization of methylene blue (MB) solution in merely 5 minutes, which is a 28-fold acceleration compared to the untreated MG (140 minutes). The obtained extraordinary reaction rate constant of 0.751 min^{-1} outperforms currently mainstream Fe-based MG catalysts by 50% (typically < 0.5 min^{-1}). Multi-scale characterizations reveal that the UT-induced structural ordering fundamentally enhances degradation capability. High-energy X-ray diffraction, small angle neutron scattering (SANS), and high-resolution transmission electron microscope (HRTEM) collectively analyze the structural reconstruction during ordering, particularly the precipitation of nanoscale Fe and Fe_2B phases inside the stimulated MGs, which favors the formation of galvanic cells between the stable nanocrystalline and metastable high-energy amorphous matrix. Simultaneously, the UT reshaping surface morphology creates abundant channels for mass transport and electron transfer. This work pioneers an ordering strategy for catalyst design through UT-assisted structural manipulation, which demonstrates synergistic effects between microstructural optimization and morphology reconfiguration engineering. These findings not only provide experimental validation for the UT-assisted degradation mechanism but also offer a generalizable strategy for developing next-generation environmental catalysts through precise structural tailoring.

1. Introduction

With the rapid development of modern industries such as chemical engineering, advanced agriculture, and textile manufacturing, the relative water pollution issues have increasingly attracted much attention [1,2]. In particular, some colorants and azo dyes are widely applied

* Corresponding author.
E-mail address: yuanchenchenneu@hotmail.com (C. Yuan).
[1] These authors contribute equally.

https://doi.org/10.1016/j.actamat.2025.121531
Received 2 July 2025; Received in revised form 2 September 2025; Accepted 10 September 2025
Available online 11 September 2025

in these industries. It is reported that about 20% of azo dye wastewater is discharged directly into the rivers by the factories [3], which results in serious and irrevocable water pollution due to its complicated chemical compositions, high organic concentrations, and very difficult to decompose [4]. Consequently, substantial endeavors have been conducted for wastewater purification during the past decade, including physical, chemical, and biological approaches [5–7]. Unfortunately, the physical pathway only filters or separates some organic chemicals rather than totally decomposes the azo dyes by changing their intrinsic chemical characteristics [4,8], which can't fundamentally realize the purification of wastewater. Moreover, the traditional chemical or biological approaches can achieve the degradation of azo dye solution, but some disadvantages like high cost, low efficiency, and bad stability seriously restrict their wide applications [9,10]. Advanced oxidation process (AOP) is a method that generates extremely reactive radicals in order to destroy organic molecules, particularly resistant chemical compounds that are found in aqueous environments [11]. It is regarded as high-performance techniques for wastewater treatment because of their highly effective, low expensive, environmentally friendly, excellent stability, and extensive adaptability in decontamination [2,12–14]. Generally, AOPs can be categorized into ozone oxidation [15,16], photocatalysis [17,18], and Fenton/Fenton-like oxidation based on the different catalytic routes [19]. Recently, many metal catalysts have been reported for wastewater treatments [20], including natural iron minerals (e.g., pyrite (FeS_2), magnetite (Fe_3O_4), and goethite (α-FeOOH)), Fe-based nanoparticles, and even the metal-organic framework (MOF) and its derivatives like MIL(Fe)-type MOFs. Moreover, some transition-metal-based catalysts such as Cu, Co, Mn, Ce, and Cr also show great catalytic activity [21], primarily due to the fast generation of hydroxyl radicals (·OH) with a high redox potential of 1.8-2.7 V during the chemical process. Nevertheless, exploiting low-cost and high-efficiency catalysts toward azo dye degradation remains a difficult challenge.

Metallic glasses (MGs), also known as amorphous alloys, have received much research interest resulting from their superior mechanical, physical, chemical, and biological combability [22–26]. Importantly, the unique disordered structure and far-from-equilibrium state endow the excellent catalytic performances of MGs [2]. Unlike their crystalline counterparts and pure metals, MGs exhibit a higher Gibbs free energy due to the metastable feature therefore prone to chemical reactions [27]. Furthermore, MGs normally show strong electron transfer characteristics because of the atomic dense packing with abundant non-directional bonding [28,29], which also facilitates their catalytic properties. Notably, different from the crystalline alloys restricted by thermodynamics, the compositions of MGs can be more flexible and tuned to enhance their properties [30]. In addition, heterogeneous, highly unsaturated atomic coordination, and isotropic structural characterizations offer abundant catalytic active sites, demonstrating huge potential practical catalytic prospects [31]. Consequently, amorphous alloys have been adopted as high-efficiency catalysts for water splitting (e.g., hydrogen evolution reaction and oxygen evolution reaction), fuel cells, and electrochemical nitrogen fixation [32,33].

Comparing with other AOP catalysts, Fe-based MGs have aroused considerable attention owing to their excellent characteristics of thermal stability, widespread commercialization, and low cost of Fe elements [14,34]. In particular, the B element with metalloid properties that is identified to be remarkably improved the glass-forming ability (GFA), and meanwhile, it is investigated that the appropriate B addition demonstrates significant enhancement of catalytic performance in Fe-based MGs owing to its well-distributed electronic configurations [12]. Previously reported $Fe_{80}B_{20}$ MG presents 1.8 times higher degradation efficiency compared to its crystalline alloys on decolorization of direct blue 6 solution, even 89 times higher than the commercial iron powders [35]. Moreover, B and Si synergistically result in the formation of non-compact layers on the surface of samples, which accelerates electron transfer, and eventually contributing to the excellent catalytic capability. Some ternary and quaternary Fe-based MGs, like $Fe_{78}Si_8B_{14}$ (10 times higher than crystalline ribbons) [36], $Fe_{73}Nb_3Si_7B_{17}$ (200 times higher than commercial iron powders) [34], and $Fe_{76}B_{12}Si_9Y_3$ (1000 times higher than commercial iron powders) have shown excellent degradation performance [4]. The ball-milled $Fe_{73}Nb_3Si_7B_{17}$ MG presents higher catalytic activity compared to the original sample, which is attributed to the enlarged specific surface and more reactive sites [34]. The $Fe_{70}Cr_5Ni_3Mo_3W_9Si_5B_5$ MG matrix composite fabricated by selective laser melting demonstrates a high reaction rate constant of 0.586 min^{-1} and low activation energy of 46.5 kJ/mol compared to other catalysts [37]. Nevertheless, these discovered Fe-based MGs simultaneously meet the limitations of GFA, time consuming, highly expensive cost, and limited size during fabrication, which restrict their widespread application, particularly in extreme environments like ultra-high temperatures and severe corrosive environments. It has been studied that the appropriate addition of Cr into Fe-based MGs can effectively improve their GFA [38]. For instance, compared with $Fe_{80}P_{12}C_4B_4$ ($T_g = 694$ K, $\Delta T_x = 29$ K) and $Fe_{77}Mo_3P_{12}C_4B_4$ ($T_g = 702$ K, $\Delta T_x = 37$ K), the $Fe_{70}Cr_7Mo_3P_{12}C_4B_4$ MG showed better thermal stability with T_g of 728 K and ΔT_x of 42 K, which was attributed to the added Cr resulting in the strong chemical affinities between atomic pairs and local densely atomic packing [39]. More importantly, the Cr incorporation also gains the enhancement of corrosion resistance, i.e., the corrosion potential increases to -88 mV after merely 7 at. % Cr addition, which facilitates the widespread applications of these Cr-alloyed Fe-based MGs [39].

Recent studies have shown that introducing the crystalline phase into the amorphous matrix can further improve its degradation performance [40–43]. The crystallization behaviors have shown many merits in catalysis like the formation of galvanic cells and controllable crystalline structures [44]. For example, it is reported that the nanocrystal coupled with sub-nanometer clusters can accelerate the hydrogen evolution reaction by offering more hydrogen production sites [45]. However, the traditional thermal treatment method to control the growth of nanocrystals always leads to the alteration of the amorphous matrix. It is revealed that high-frequency ultrasonic treatment (UT) can remarkably affect the mechanical, thermal, and anti-corrosion properties of MGs by directly injecting the energy into the amorphous matrix [46–48]. Previously, our group successfully realized the enhancement of plasticity of the medium-entropy $La_{55}Al_{25}Ni_5Cu_{10}Co_5$ MG by the UT-induced structural ordering [25]. Meanwhile, the micro-forming, welding, fabrication, and accurate processing of MGs subjected to UT were widely investigated [49]. Moreover, the external conditions (e.g., stress or temperature) enable MGs away from their equilibrium state to achieve the structural transition like relaxation/aging or rejuvenation [50–52]. Nevertheless, how the intrinsic structural order of MGs evolves under UT, and especially how the structural ordering impacts the degradation behavior is rarely revealed.

Herein, we reported a novel $Fe_{76}Cr_2Si_{11}B_{11}$ MG catalyst treated by ultrasonic mechanical vibration with different times as catalysts for degrading azo dye solution, where the methylene blue (MB) was taken as example. It is found that the variation of structural order affected by UT significantly improves the degradation performance with a reaction efficiency approaching 0.751 min^{-1}, outperforming currently mainstream Fe-based MG catalysts (normally < 0.5 min^{-1}) by 50%. Based on the detailed analyses of the surface morphology, structural order, chemical state, and crystallization behaviors, the degradation mechanism of UT $Fe_{76}Cr_2Si_{11}B_{11}$ MG catalysts was systematically investigated, which potentially provides a new insight into the design of highly efficient catalysts from the perspectives of microstructural optimization and surface morphology reconfiguration engineering.

2. Experimental procedures

2.1. Materials preparation

The amorphous powders with a composition of $Fe_{76}Cr_2Si_{11}B_{11}$ (at. %) (as-cast) were purchased commercially to serve as pre-fabrication materials for the degradation experiment. These amorphous powders were ultrasonically vibrated by BRANSON 2000X ea/ae with a frequency of 20 kHz under the processing times of 0.489, 0.665, 1.029, 1.170, 1.878, and 2.713 s, which correspond to the applied energies of 500, 750, 1000, 1250, 2000, and 3000 J, respectively (conveniently named as 0 (as-cast), 500, 750, 1000, 1250, 2000, and 3000 J samples). The trigger force was 50 N, the vibrated amplitude was 44.4 μm, and the pressure of the working cylinder was 400 kPa.

2.2. Materials characterizations

The amorphous characteristics of original and vibrated samples were examined by X-ray diffraction (XRD, D8 advance, Bruker) with Cu Kα radiation (λ = 0.15405 nm). The XRD patterns were recorded by measuring angle ranges of 10-80° with a scanning interval of 0.02°. Different from the crystalline alloys that their structure can be identified by lattice parameters, the microstructure of MG is frequently described by using the following statistical parameters, including structure factor $S(q)$, reduced pair-distribution function $G(r)$, and pair correlation function $g(r)$ [53]. In this study, a series of high-energy XRD experiments were performed, along with a maximum wave vector momentum transfer of $q = 9$ Å^{-1}. Subsequently, the 2D images were integrated with the software of Fit2D and Dioptas. $S(q)$ is the Fourier transform of the pair correlation function $g(r)$, describing how the intensity of scattered radiation (X-rays/neutrons) varies with the scattering vector q (where $q = 4\pi\sin\theta/\lambda$, with θ being the scattering angle and λ the wavelength) [54]. The reduced pair distribution G(r) was obtained via using the program package PDFgetX3, which is derived from the following equation [54]:

$$G(r) = \frac{2}{\pi}\int_0^\infty q[S(q)-1]sin(qr)dq \quad (1)$$

The $g(r)$ can be calculated from the experimentally determined $G(r)$, which is expressed by [55]:

$$g(r) = \frac{G(r)}{4\pi\rho_0 r} + 1 \quad (2)$$

where the ρ_0 is the mean atomic number density of the alloy, which can be approximately obtained by the weighting average density of each atom in this study.

Small angle neutron scattering (SANS) experiments were conducted at small angle neutron diffractometer at China Spallation Neutron Source (CSNS). The incident neutron wavelength of 3 - 8.6 Å was determined by the double-disc bandwidth chopper, collimating to the sample through a pair of apertures. The sample aperture size and sample-to-detector distance were configured as 8 mm and 5 m, respectively, and the scattering information was collected approximately for 50 minutes for each sample during the experiment, including the empty sample holder (double-layer quartz glass) and the sample cell. Besides, utilizing two-dimensional ^{3}He tube array detector to cover a Q range from 0.004 to 1.2 Å^{-1}. After normalization, transmission correction, and standard sample calibration, the scattering data were set to the absolute unit for further analysis. The scanning electron microscope (SEM, Hitachi Regulus 8100, Japan) equipped with an energy dispersive X-ray spectrometer (EDS) was utilized to observe surface morphology and elemental distribution of samples. The Brunauer-Emmett-Teller (BET) surface area measurements of the MG powders before and after UT were performed by using N_2 adsorption method with a surface analyzer (Micromeritics ASAP 2460) under the testing temperature of 77.3 K. The detailed microstructure of samples was analyzed by using a high-resolution transmission electron microscope (HRTEM, Talos F200X) with an accelerating voltage of 200 kV. Specifically, to quantitatively estimate the structural order of the sample. We have selected a random region with the size of 20 × 20 nm^2 from the HRTEM image, and then divided it into 100 cell units with a size of 2 nm × 2 nm to close to the smallest size of the observed crystal order [56]. Subsequently, the short-range order of each cell by employing two-dimensional autocorrelation functions (2D ACFs). Based on the concept that the ordered cell normally exhibits crystal-like properties, such as a significant lattice fringe or symmetry [57,58]. The areal fraction of the short-range order of the sample can be approximately determined. The chemical states of samples were measured via X-ray photoelectron spectroscopy (XPS, Thermo Scientific ESCALAB 250Xi, America). The degradation products of MB solution treated with $Fe_{76}Cr_2Si_{11}B_{11}$ MG powders were performed by Fourier-transform infrared (FTIR) (Thermo Scientific Nicolet iS10) measurements in the wavelength range of 400 - 4000 cm^{-1}, and the empty chamber was adopted as a baseline before performing the FTIR measurement.

2.3. Dye degradation measurements

Utilizing deionized water to prepare a 250 mL MB solution with a concentration of 100 mg/L in a 500 mL beaker, H_2O_2 was added to adjust the concentration to 5 mM, then 0.1 M H_2SO_4 and 0.1 M NaOH solutions were used to realize the adjustment of pH values of the solution. The beaker with dye solution was subsequently placed in a thermostatic water bath, and the temperature of the solution was stably maintained at a room temperature of 298 K under a heat controller. Afterwards, the original and treated (500, 750, 1000, 1250, 2000, and 3000 J) $Fe_{76}Cr_2Si_{11}B_{11}$ samples were added as catalysts for degrading the MB solution. To avoid the influence on degradation performances due to the aggregation of samples, the solution was mechanically stirred by using a stirrer with a fixed speed of 450 r/min during degradation. Finally, 3 mL aqueous solutions were taken out by using a syringe and filtered through a membrane with a diameter of 0.22 μm at selected time intervals, and then injected into a transparent cuvette to measure their absorbance spectrum with the wavelength range of 200-800 nm by using an ultraviolet-visible (UV-vis) spectrophotometer (Shimadzu UV-1280).

3. Results and discussions

3.1. UT processing and structure reconstruction of samples

Fig. 1(a, b) and the corresponding insets show the surface morphology of the 0 and 1250 J samples, respectively. It is found that the surface morphology of the original sample is smooth and clean without any significant defects such as pores and cracks, as shown in Fig. 1(a). In addition, the EDS measurement (see the summarization in Table S1) indicates O elements appear on the particle surface due to the formation of thick oxide layers that originate from the preparation and long-time reserving, which might obstacle the contact between the azo dye solution and MG catalyst. In contrast, the particle surface morphologies of powders become rougher after UT at a processing time of 1.170 s. Besides, some irregular morphologies like ellipsoidal and dumbbell-like shapes appear in the 1250 J sample, along with some small pillars, protrusions, and microcracks emerging on the particle surface, as illustrated in Fig. 1(b). The average particle distribution sizes of 0 and 1250 J samples are shown in Fig. 1(c) and (d), respectively. It is found that the particle size significantly increases after UT, which is mainly ascribed to the jointing of the isolated particles induced by the UT-assisted welding process [59]. Although the O elements are also detected on the particle surface, these protrusions and microcracks probably facilitate the enlargement of reaction-contacted areas during degradation and overcome the negative impact of oxide layers.

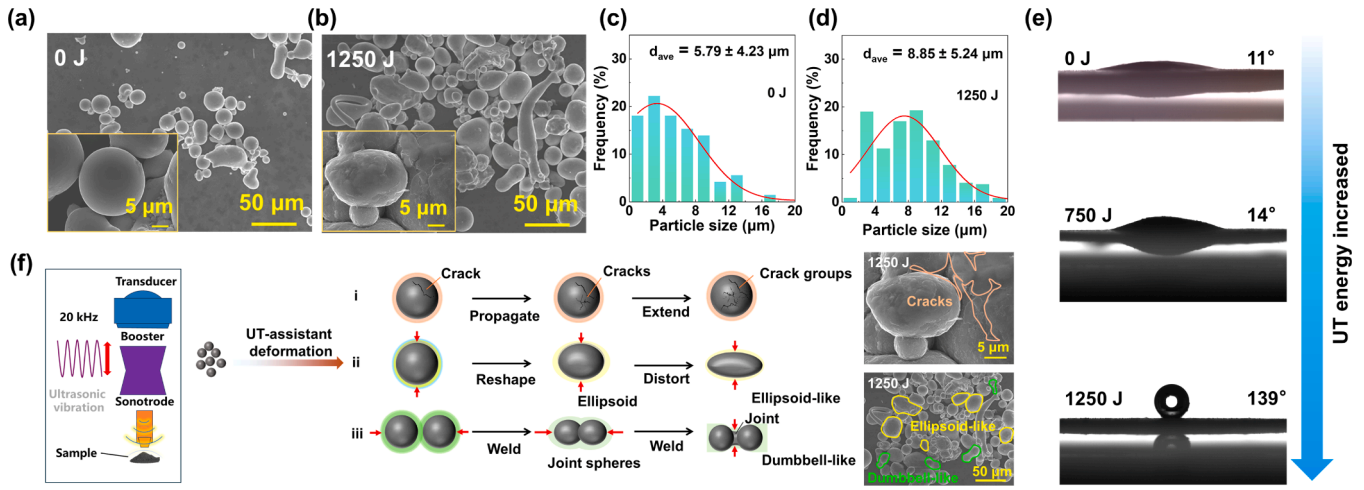

Fig. 1. (a, b) SEM images of the surface morphology for 0 (a) and 1250 J (b) samples under different scanning bars. (c, d) Statistics of particle size distribution for the 0 (c) and 1250 (d) J samples. (e) Water contact angles of the selected 0, 750, and 1250 J $Fe_{76}Cr_2Si_{11}B_{11}$ MGs. (f) Schematic illustration of the ultrasonic treatment equipment (left panel). Illustrations of the reconfiguration of surface morphology of the sample under UT (medium panel), and the representative SEM images (right panel) of the 1250 J sample are depicted for clear demonstration.

Subsequently, to further validate the variation of surface morphologies, the images of a water droplet on the aggregated $Fe_{76}Cr_2Si_{11}B_{11}$ powders are demonstrated in Fig. 1(e). The corresponding water contact angles are determined to be 11°, 14°, and 139°, respectively, at UT processing times of 0, 0.665, and 1.170 s. It is suggested that the aggregated powders exhibit a typical transition from intrinsic hydrophilicity to hydrophobicity owing to the UT-enhanced surface roughness along with multiscale defects as indicated by Fig. 1(b) and Fig. S1. Fig. 1(f) vividly depicts the particle deformation during the UT process. The left panel exhibits schematics of a typical UT device, including a transducer, booster, and sonotrode, in which the transducer can convert high-frequency ultrasonic signals into mechanical vibrations, and then the booster amplifies the amplitude of the vibration, finally the sonotrode can enlarge the vibrated amplitude and concentrate the vibration energy on the contact surface to achieve the processing of samples [47]. The right panel of Fig. 1(f) illustrates the UT-induced deformation

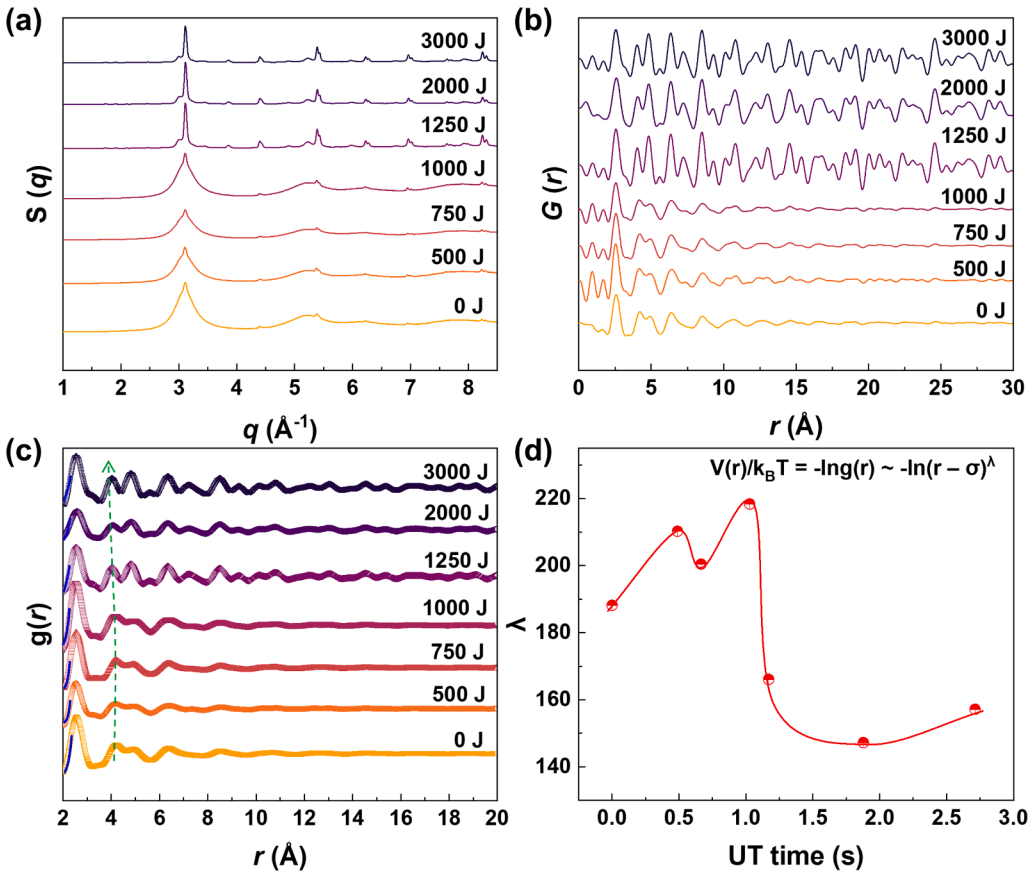

Fig. 2. (a) S (q), (b) G (r), and (c) g(r) curves of 0, 500, 750, 1000, 1250, 2000, and 3000 J $Fe_{76}Cr_2Si_{11}B_{11}$ samples under UT at different energies. (d) The obtained value of repulsion steepness (λ) of the sample under UT by fitting the left flank of g(r) curves.

process, which can be categorized into three parts: (1) the single crack appears on the surface of particles when the sample is subjected to UT, subsequently this crack propagates to multi-cracks with increasing processing time, and finally transforms to several crack groups on the surface. (2) Part of spherical particles are reshaped into ellipsoids due to UT, and then these ellipsoids are gradually distorted into ellipsoid-like shapes due to the continuous vibration. (3) The separated particles are welded together under UT. Due to the UT-assistant welding process, these joint spheres gradually transform into a dumbbell-like shape. This is consistent with the previously reported works that UT can be used as the high-efficiency approach to join MGs or amorphous composited materials [48]. Moreover, the BET specific surface areas of the sample before and after UT are conducted by using the N_2 adsorption-desorption method, as illustrated in Fig. S2. It is found that the N_2 adsorption of the 1250 J MG is much stronger than the original sample, and the corresponding specific surface area is calculated to be 2.016 m^2/g, which is 9.25 times higher than the 0 J MG (0.218 m^2/g). Accordingly, the specific surface area of MGs remarkably expands after UT. These results imply the UT-optimized 1250 J MG catalyst possesses a large specific surface area, which can provide more active sites and facilitate the interaction between catalyst and MB solution during degradation.

The amorphous nature of as-cast (0 J) $Fe_{76}Cr_2Si_{11}B_{11}$ samples was checked before UT, as depicted in Fig. S3. Some crystallized phases like Fe and Fe_2B appeared in the XRD patterns due to the long-time UT process. To obtain more detailed structural signatures, a series of high-energy XRD measurements were conducted, see Fig. 2 (a-d). Fig. 2(a) gives the $S(q)$ curves of all samples. As compared with the 0 J sample (0.37 $Å^{-1}$), the first peaks of $S(q)$ for 500, 750, and 1000 J samples (in the range of 0.32-0.34 $Å^{-1}$) become slightly narrow, which might be ascribed to the annihilation of inherited clusters from melts during the UT-induced ordering process as illuminated in Fig. 2(a). The curves of Fourier-transformed reduced $G(r)$ for the sample under UT at various times are demonstrated in Fig. 2(b), which provide the structural information in real space based on the probability distribution of interatomic pair correlations [60]. It is clear that $G(r)$ curves of 0, 500, 750, and 1000 J samples show damping of oscillations similar to metallic melts, indicating their dominantly disordered configurations. Subsequently, the $G(r)$ curves of 1250, 2000, and 3000J samples demonstrate strong damping of oscillations with increasing UT times even at a long-distance region. These notable variations suggest that the atomic structure of samples gradually becomes ordered under UT.

The obtained $g(r)$ curves of the sample under UT at different times are illustrated in Fig. 2(c). The first peak of $g(r)$ for 0, 500, 750, and 1000 J samples barely changes, exhibiting typical liquid behaviors [61]. With further increasing UT time, some peaks representing the medium-range order of above 10 Å appear, indicating more short-to-medium range ordered configurations. It is reported that the potential of mean force between two atoms is associated with the radial distribution function [62]: $V(r)/k_BT = -\ln g(r) \sim -\ln(r-\sigma)^{\lambda}$, where k_B is the Boltzmann constant, σ refers to the mutual separation between two ions that the interaction energy is practically infinite, the power exponent λ is the interatomic repulsion parameter. If the separation is very limited, $V(r)$ reduces to the short-range part of the ion-ion repulsion. Therefore, the λ represents the steepness of the effective repulsion, i.e., the larger the λ, the stronger the repulsion between atoms [63], which can be obtained by fitting the left flank of $g(r)$ using above equation. Accordingly, the $g(r)$ curves together with their corresponding linear fitting are demonstrated in Fig. 2(d), where the obtained λ are plotted in Fig. 2(d). It is observed that the λ increases to 218.35 (1000 J) as the UT time approaches 1.029 s, and then sharply drops to 147.24-166.07, when the UT time continuously increases from 1.170 to 2.713 s (e.g., $\lambda_{1250} = 166.07$, $\lambda_{2000} = 147.24$, $\lambda_{3000} = 157.15$). The pronounced steep repulsion as demonstrated in the 1000 J sample normally corresponds to a loose atomic packing, i.e., a positive excess volume [64], indicating the structural rejuvenation under UT as found in our previous work as well [65,66], which leads to the fast motion of atoms and thereby the UT-assistant ordering accompanies with newly constructed clusters. Meanwhile, the second neighboring peaks shift to a smaller position with increasing UT time (see the dotted line arrow), confirming that the samples after the long-term UT (1250, 2000, and 3000 J) exhibit denser packing induced by ordering.

HRTEM is further employed to monitor the evolution of microstructure under UT. Fig. 3(a), (b), and (c) illustrate the TEM images of 0, 1000, and 1250 J samples, respectively. Their corresponding selected area electron diffraction (SAED) patterns are demonstrated in Fig. 3(d), (e), and (f), respectively. It is found that the SAED of the 0 J sample exhibits a significant halo, further confirming its amorphous nature. In contrast, as the UT time increases to 1.029 s, minor bright spots appear in the SEAD pattern of 1000 J sample, suggesting the enhancement of structural order although the whole system is still in an amorphous state. Notably, significant crystalline phases precipitate within the amorphous matrix, and diffraction rings with spots corresponding to the (110), (200), and (211) planes of Fe and Fe_2B phases clearly emerge. Fig. 3(g) shows the HRTEM image of the 1250 J sample, some remarkable lattice fringes appeared, as indicated by red (A) and blue (B) squares. The corresponding lattice spaces are determined to be 2.024 and 1.426 Å, which represent to the lattice planes of (110) and (200), respectively. The result indicates that the UT induces remarkable crystallization behaviors of samples, which is consistent with the XRD results.

3.2. Degradation performances, chemical state, and surface morphologies of UT MGs

3.2.1. Degradation performance

A series of degradation experiments of MB solution were conducted to investigate how the UT-induced ordered structure influences the degradation behavior, see details in Fig. S4. Fig. 4(a) and (b) present the typical two-dimensional UV-vis spectra of MB solution treated by 0 and optimal 1250 J $Fe_{76}Cr_2Si_{11}B_{11}$ MGs at room temperature, respectively, in which the maximum absorbance peak of 653 nm is attributed to the n-π^* transition of the chromophore bond [67], the intensity of which represents the concentration of solution. It is found that the characteristic peak intensity of MB solution by using as-cast MGs slowly decreases with treatment time and the whole degradation process exceeds 140 minutes, as depicted in Fig. 4(a). In contrast, a significant decolorization behavior occurred during the Fenton-like reaction treated with the 1250 J sample, along with the degradation consuming time of only 5 minutes which is about 28 times shorter than that of the as-cast sample, see Fig. 4 (b) and the corresponding inset. The digital images of complete decolorization of MB solution during the degradation process are shown in Fig. S5. To compare the degradation capability of $Fe_{76}Cr_2Si_{11}B_{11}$ MGs after UT at different times, the C_t/C_0 as a function of time in MB solution treated by 0, 500, 750, 1000, 1250, 2000, and 3000 J samples is illustrated in Fig. 4(c), where C_t and C_0 denote to the instant and initial concentration. It is observed that the 0 J sample exhibits extremely limited degradation capability with the C_t/C_0 barely changed within 30 minutes, while the sample presents notable degradation performance after UT. As the UT time increases from 0 to 1.170 s, the degradation capability of the sample gradually increases, reaching the highest value, and then slightly decreases with further ascending UT time. Furthermore, it is noted that the concentration of MB solution for both 0, 500, 750, and 1000 J samples barely changes during the initial period, which is primarily ascribed to the time required for the generation of ·OH and the ·OH groups approaching organic chromophore molecules [14]. The Fenton-like reaction obeys the pseudo-first-order decay kinetic model, and its degradation kinetics can be disclosed by fitting the degradation efficiency with reaction time via the following equation [68]:

$$C_t = C_0 exp(-kt) \quad (3)$$

where k is the reaction rate constant, and t represents the degradation time. Fig. 4(d) plots the $\ln(C_0/C_t)$ as a function of t for MB solution

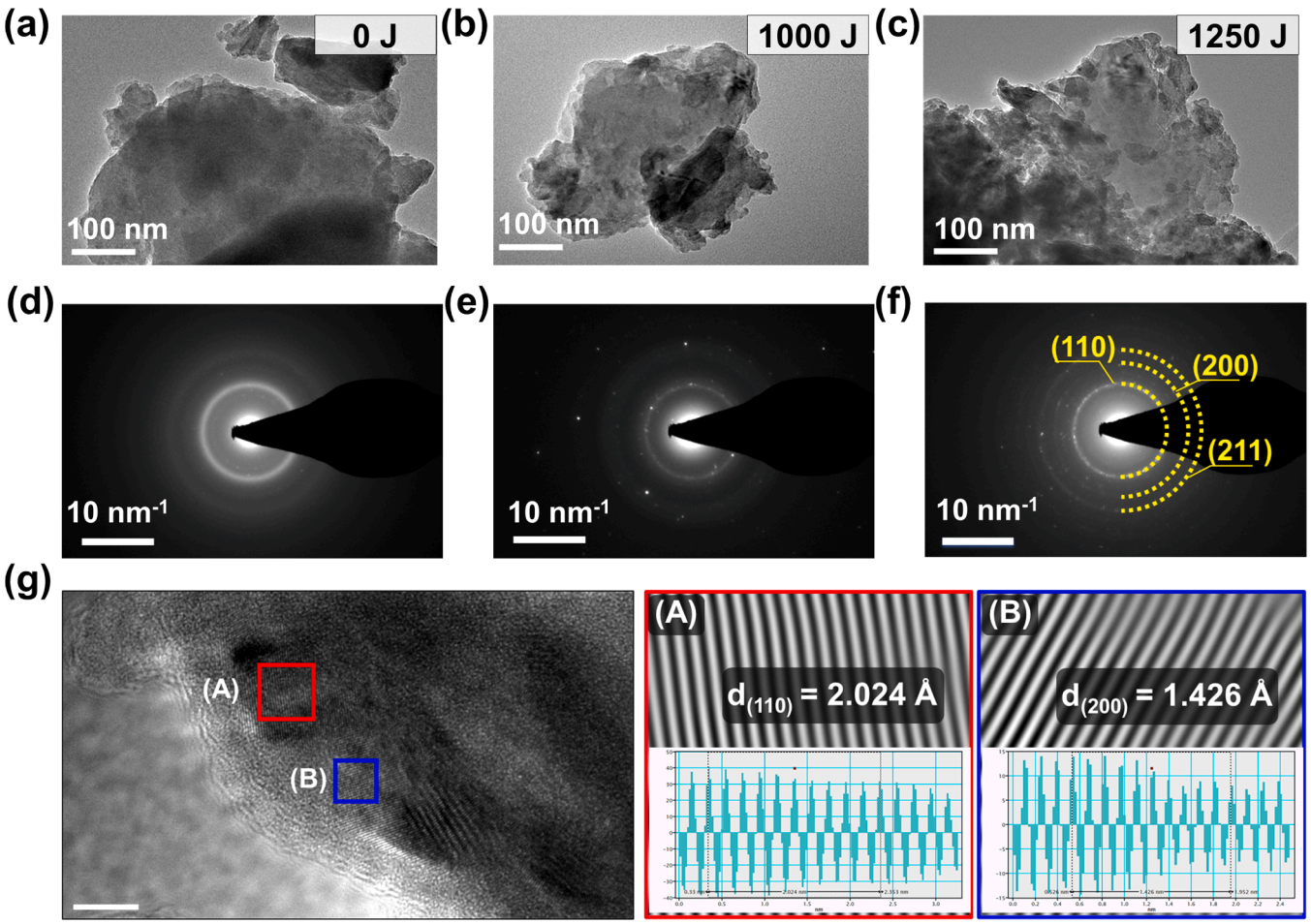

Fig. 3. (a-c) HRTEM images of 0 (a), 1000 (b), and 1250 J (c) $Fe_{76}Cr_2Si_{11}B_{11}$ MGs. (d-f) The SAED patterns of 0 (d), 1000 (e), and 1250 J (f) $Fe_{76}Cr_2Si_{11}B_{11}$ samples, respectively. (g) The HRTEM image of the 1250 J sample, along with selected areas with significant lattice fringes, which are marked by green and blue squares (A and B).

treated by 0, 500, 750, 1000, 1250, 2000, and 3000 J samples, where the corresponding reaction rate constant *k* can be derived by linear fitting of the experimental data. It is found that the 0 J sample exhibits *k* with an extremely low value of 0.001 min^{-1} that approaches zero. In contrast, the *k* is significantly improved after UT, especially for the 1250 J sample with the highest *k* of 0.751 min^{-1} among these studied samples (750 times of the as-cast one), then gradually decreases with further increasing time, ultimately determining to be 0.520 min^{-1} at the UT time of 2.713 s.

In order to demonstrate the reusability of the UT-optimized 1250 J MG catalyst, the corresponding MB solution degradation cycling test is performed, as shown in Fig. 4(e). It is found that the degradation time gradually increases with ascending reusability of the sample. The MG catalyst realizes the complete decolorization of MB solution within 10 minutes at 11^{th} run, which is only 5 minutes slower than the 1^{st} run. With further increasing the number of cycles, the degradation time significantly increases, and the sample consumes 30 minutes to achieve absolute degradation, which is much better than many reported Fe-Si-B series MG catalysts, such as $Fe_{73.5}Si_{13.5}B_9Cu_1Nb_3$, $Fe_{78}Si_{11}B_9P_2$, $Fe_{78}Si_9B_{13}$, $Fe_{76}Si_{7.6}B_{9.5}P_5C_{1.9}$ [69–72]. Nevertheless, because of difficulty and complexity in recycling of MG powders, the cycling testing for the 1250 J $Fe_{76}Cr_2Si_{11}B_{11}$ MG only conducts 21 times. Moreover, we have also successfully performed additional dye degradation treated with 1250 J MG powders, including Orange II, Rhodamine B, and the mixtures of these dyes, as demonstrated in Fig. S6, which illustrates their universally applicable catalytic capability.

Additionally, to demonstrate the excellent catalytic performance of our as-prepared catalyst, we have compared the *k* value between the UT-optimized 1250 J $Fe_{76}Cr_2Si_{11}B_{11}$ MG and other reported Fe-based MG catalysts, see the summarization in Fig. 5 and Table S2 [14,28,35,36,69,71,73–93], the outstanding *k* value indicating its extraordinary degradation capability. Obviously, the UT accelerates the degradation reaction process and effectively enhances the degradation efficiency of MGs. To give a deep understanding of the UT-assisted degradation mechanism of MGs, we further investigated their surface morphology, electronic structure, microstructure, potential energy changes, etc.

3.2.2. *Chemical state and electrochemistry analysis*

It is generally accepted that the Fenton-like degradation process with Fe-based MGs has been revealed by following steps [14]:

$$Fe^0 + H_2O_2 \rightarrow Fe^{2+} + 2OH^- \quad (4)$$

$$Fe^{2+} + H_2O_2 \rightarrow Fe^{3+} + \cdot OH + OH^- \quad (5)$$

$$OH + \text{organics} \rightarrow \text{products} \quad (6)$$

As can be seen that the H_2O_2 reacts with the Fe^0 on the surface of the $Fe_{76}Cr_2Si_{11}B_{11}$ MG for generating Fe^{2+}, which facilitates the acceleration of the following Fenton-like chemical reaction [14]. To deeply understand the degradation mechanism of $Fe_{76}Cr_2Si_{11}B_{11}$ MGs before and after UT, their corresponding XPS spectra are detected, see details in Fig. S7. Fig. 6(a) shows the Fe 2*p* XPS spectrum of the as-cast MG sample before and after degradation, it is found that the spectrum is deconvoluted into three peaks, corresponding to 707.77, 710.89, and 712.43 eV,

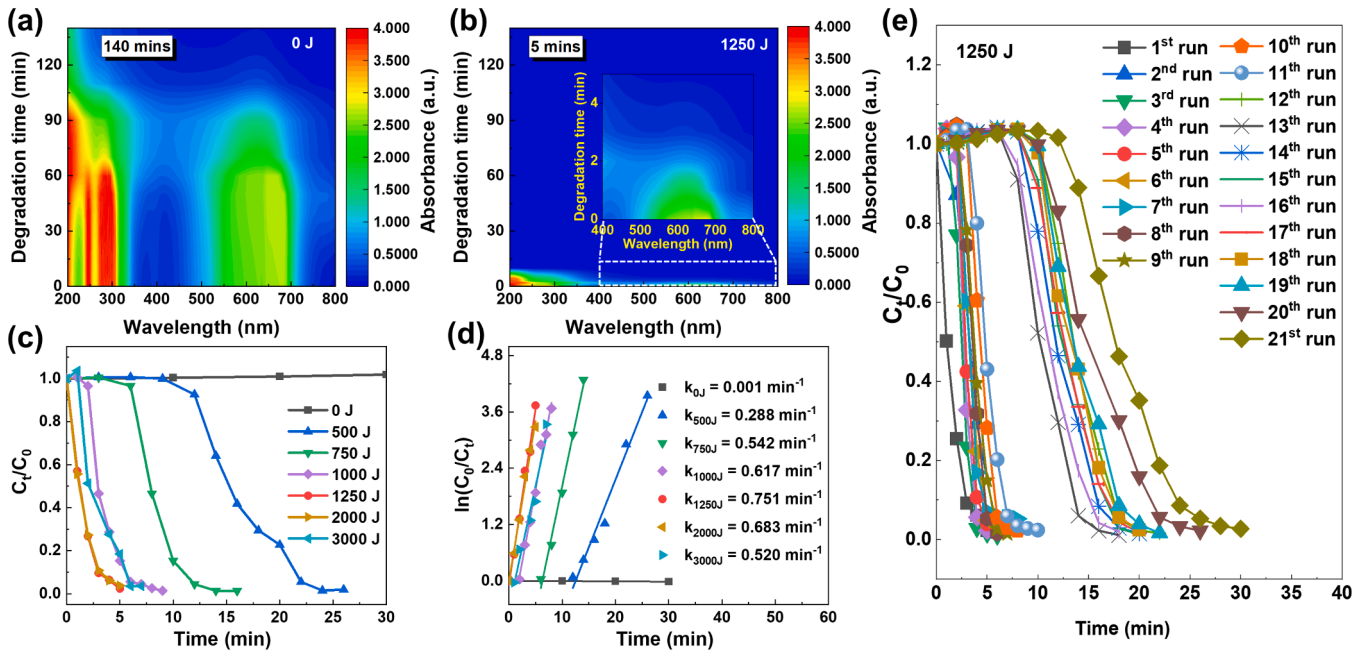

Fig. 4. (a, b) The UV-vis spectra of the MB solution treated with the 0 (a) and the optimal 1250 J (b) samples, the inset in (b) demonstrates the enlarged spectrum in the wavelength range of 400-800 nm. (c) C_t/C_0 as a function of degradation time for 0, 500, 750, 1000, 1250, 2000, and 3000 J samples. (d) The linear fitting of ln (C_0/C_t) versus degradation time for $Fe_{76}Cr_2Si_{11}B_{11}$ samples. (e) C_t/C_0 as a function of time for the $Fe_{76}Cr_2Si_{11}B_{11}$ MG catalyst during degradation under each reusability.

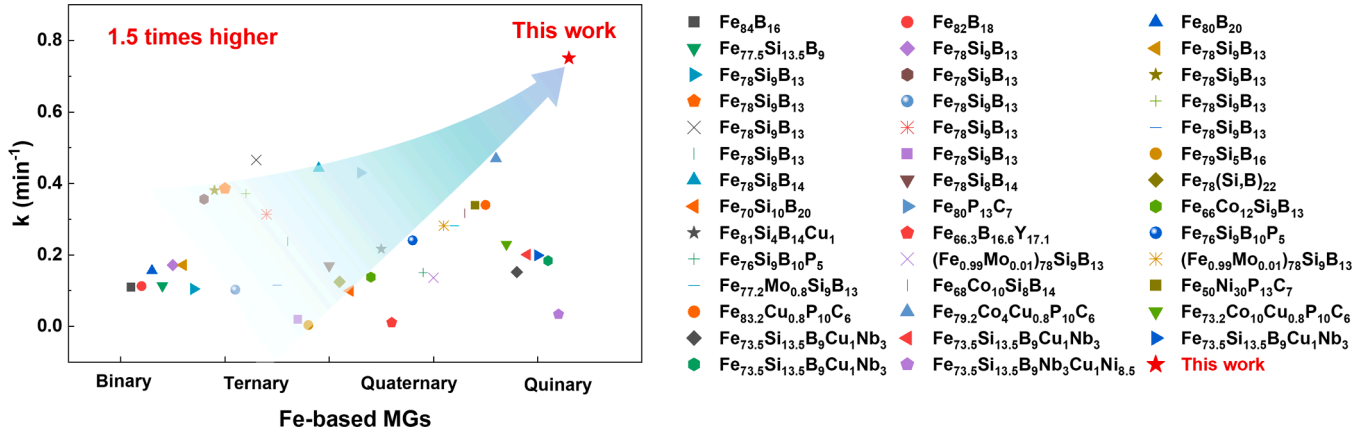

Fig. 5. The summarization of k for the 1250 J $Fe_{76}Cr_2Si_{11}B_{11}$ MG and previously reported Fe-based MGs [14,28,35,36,69,71,73–93].

which are assigned to states of Fe^0, Fe^{2+}, and Fe^{3+} ions, respectively. Notably, Fe^0 almost disappears after degradation (see Table S3), indicating that Fe^0 was oxidized during the degradation process. Meanwhile, the total amount of Fe on the sample after degradation (15.52%) is lower than the fresh sample (16.16%), as listed in Table S4, suggesting that the Fe participates in the degradation of MB solution, which coincides with the EDS analysis that the content of Fe shows a significant reduction during the degradation process. Besides, to investigate the variation of the Fe chemical state for the sample after UT, Fig. 6(b) demonstrates the Fe 2*p* spectrum of the 1250 J sample. Similar to the observation from the surface of the original sample, Fe 2*p* spectra of the 1250 J MG that are deconvoluted into three peaks at 707.07, 710.01, and 711.49 eV, which are ascribed to the metallic states of Fe^0, Fe^{2+}, and Fe^{3+}, respectively. Interestingly, it is found that the intensified Fe^0 state appears in the $Fe_{76}Cr_2Si_{11}B_{11}$ MG after UT at a processing time of 1.170 s compared to the untreated sample. The increment of content of Fe^0 facilitates the generation of Fe^{2+} during the Fenton-like process, see formula 4. Moreover, it is noteworthy that the Fe^{2+} 2*p* position of the 1250 J sample shifts to a lower value of 710.01 eV compared with the original MG (710.89 eV), suggesting that the occurrence of strong electron transfer inside MG samples after UT [44]. The rest of the elemental XPS spectra and corresponding discussions are demonstrated in Figs. S8 and S9.

In addition, the catalytic degradation behaviors of materials are closely associated with their electron transfer [28]. As such, Fig. 6(c) demonstrates potentiodynamic polarization curves of 0, 1000, and 1250 J samples in an open circuit potential after stabilization. It is found that the negative corrosion potentials of 0, 1000, and 1250 samples are determined to be -0.33, -0.22, and -0.04 V_{SCE}, respectively. The lowest potential of the 0 J sample indicates its stronger corrosion trends and poor surface stability. In contrast, the 1250 J sample shows a higher potential, suggesting its better corrosion resistance compared with others. Furthermore, the electrochemical impedance spectroscopy (EIS) spectrum for these studied samples in the frequency ranges of 0.01-1000 kHz is depicted in Fig. 6(d). The inset shows the simplified equivalent circuit for the EIS data fitting, the corresponding fitted results are listed

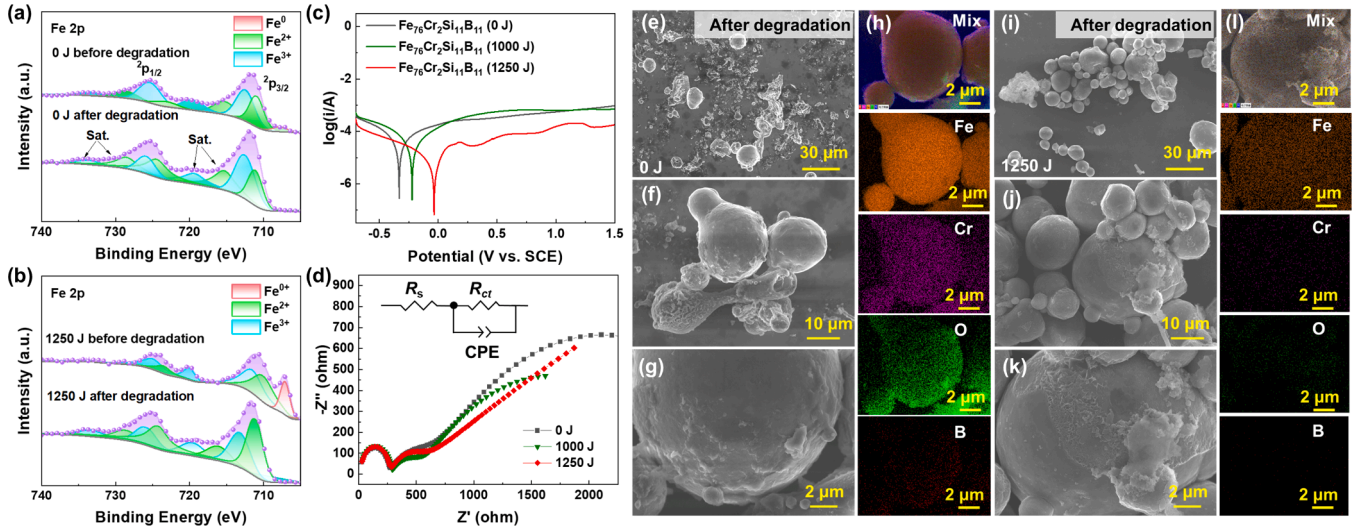

Fig. 6. (a, b) XPS spectra of Fe 2*p* of 0 (a) and 1250 J (b) samples before and after degradation. (c, d) The polarization curves (c) and (d) EIS measurements of 0, 1000, and 1250 J samples, the inset shows the general fitted circuit. Powder particle surface morphology of the 0 J (e-g) and 1250 J (i-k) samples after degradation under different scanning bars, the corresponding elemental mappings are exhibited in (h) and (l), respectively.

in Table S5. It can be seen that all samples exhibit a smaller semicircle with the passivated film impedance. Intriguingly, the 1250 J sample demonstrates a smaller secondary semicircle compared with the original sample, indicating a low electron transfer impedance that a rapid electron transfer occurs in the 1250 J sample, which facilitates the acceleration of the Fenton-like reaction, ultimately contributing to the better degradation performance.

3.2.3. *Surface morphology after degradation*

The degradation performance of MGs is strongly associated with their surface morphology due to the fact that the catalytic reaction is a surface-mediated process [94]. Because of UT, the separate particle experiences different deformations, like the appearance of cracks, ellipsoid-, and dumbbell-like shapes, as shown in Fig. 1(f) and Fig. S1. Fig. 6(e-l) illustrates the surface morphologies and elemental distribution of the selected 0 and 1250 J samples after degradation. The surface elemental mapping of the 0 J sample after degradation is detected by EDS, as illustrated in Fig. 6(h). Each element is uniformly distributed on the particle surface, the O element content of the 0 J sample is determined to be 36.6% due to the large amount of oxide layers formed on the surface, and the content of Fe is also consumed because of the Fenton-like reaction, as summarized in Table S1. Comparing with the original powder, the particle surface of the 1000 and 1250 J samples exhibits flocculent-like fragments, as shown in Fig. S10 and Figs. 6(i-k), respectively. Such flocculent-like morphologies not only enlarge the contact area between catalysts and MB solution, thereby accelerating the degradation process [14], but also effectively improve corrosion resistance, as shown in Fig. 6(c). Moreover, as shown in Fig. 6(l), the element mapping and statistics revealed an 11.9% reduction in Fe content and a 14.2% increment in O content for 1250 J after the reaction due to the gradual consumption of Fe to produce •OH, which in turn facilitates the dye degradation process. Notably, there are no significant Fe metal aggregations in the MG catalyst after degradation as revealed by the SEM images. Moreover, EDS mapping demonstrates that all elements, particularly metallic Fe and Cr, remain uniformly distributed across the particle surface. This homogeneous dispersion suggests that no noticeable metal leaching phenomenon occurred during degradation. Meanwhile, it is observed that the hydroxylated intermediates like •OH may exist in the MB solution after degradation due to the O-H stretching vibration peaks at ~3410 cm^{-1} in the FTIR spectrum, which suggests the appearance of radical active species during degradation, as illustrated in Fig. S11.

3.3. *Evolution of structural order*

To accurately characterize the internal microstructure of MG samples and track its evolution during the UT-induced ordering processing, SANS measurements as advanced nanostructured characterization technology are employed, which are frequently used to detect the structural heterogeneity of chemical composition, density, and magnetism from 1~100 nm in the material. Besides, SANS also can reveal nanoscale structural evolution [95,96]. As a typically non-destructive method, SANS provides statistically representative data from a large volume, making it highly efficient for the characterization of bulk sample. Herein, we further adopt a series of SANS measurements to acquire more detailed structural information of samples before and after UT. Fig. 7(a), (b), and (c) demonstrate 2D SANS patterns of 0, 1000, and 1250 J MGs (the data of other samples are shown in Fig. S12), respectively. The SANS intensity of MGs significantly increases within the *Q* range of ± 0.005 nm^{-1}, meanwhile the 1250 J sample exhibits stronger SANS intensity compared with the original sample, indicating the intensified structural inhomogeneity of samples after UT. Fig. 7(d) gives experimental SANS profiles collected at 50 mins in the *Q* range of 0.0045-0.1 $Å^{-1}$ for 0, 500, 750, 1250, and 2000 J $Fe_{76}Cr_2Si_{11}B_{11}$ MGs. It is worth noting that the SANS intensity gradually increases with ascending UT time from 0 to 1.170 s, and decreases slightly with further increasing time to 1.878 s. Normally, the crystallized samples show higher SANS intensities than their corresponding amorphous counterparts, as seen in the previously reported $Pd_{41.25}Ni_{41.25}P_{17.5}$ MG [97]. In our study, the UT-induced structural transition from a fully amorphous state to a more ordered state, involved some significant nanocrystal precipitation within the amorphous matrix. This transition, evidenced by XRD and HRTEM analyses above, leading to the enhanced SANS intensity, as illustrated in Fig. 7(e), particularly noticeable for 1250 and 2000 J MGs within the range of 0.02-0.05 $Å^{-1}$. To explore the size evolution of crystalline precipitates of the sample during the UT process, SANS profiles are fitted with a model of the lognormal size distribution of spherical particles and a flat background, which is expressed by [98]: $f(r) = \left(1/\sigma R\sqrt{2\pi}\right) \times \exp\left[-(lnR - lnR_{med})^2/2\sigma^2\right]$, where $f(r)$ is the size distribution function, R_{med} and σ represent the median radius and polydispersity of the crystalline precipitates, respectively, and the corresponding specific value can be obtained based on the fitted results. The temporal evolution of the R_{med} for the sample under different UT times is illustrated in Fig. 7(f), it is viewed that the R_{med} increases from 47.60 to

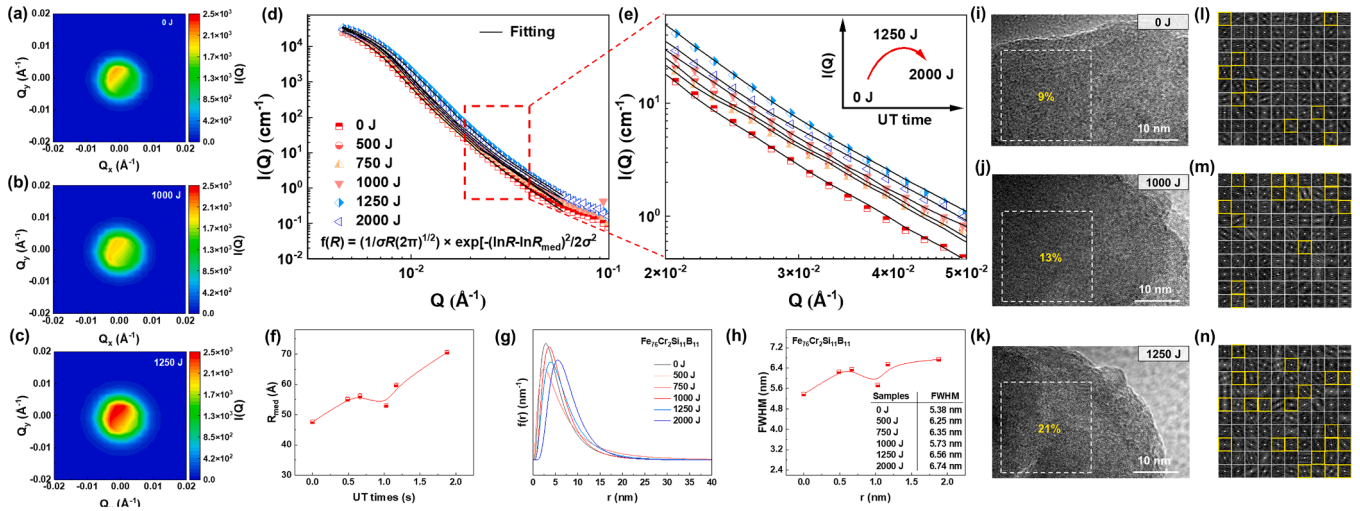

Fig. 7. (a, b, c) 2D SANS patterns of 0, 1000, and 1250 J samples. (d) Experimental SANS scattering profiles of 0, 500, 750, 1000, 1250, and 2000 J $Fe_{76}Cr_2Si_{11}B_{11}$ MG powders, along with the linear fittings obtained by the log-normal size distribution function. (e) Magnified view of SANS profiles with the Q range of 0.02-0.05 Å^{-1}. (f) Temporal evolution of median particle radius R_{med} for the sample during the UT process. (g) Particle size distribution curves of 0, 500, 750, 1000, 1250, and 2000 J samples. (h) FWHM of the size distribution curve for the sample under UT at different times. (i-k) HRTEM images of 0 (i), 1000 (j), and 1250 J (k) samples, the corresponding selected squares of 20 nm × 20 nm are marked by white dash boxes. (l-n) 2D ACFs of 0 (l), 1000 (m), and 1250 J (n) samples, the size of each cell is 4 nm^2.

70.56 Å with ascending UT time, indicating the fast growth of these precipitates during UT. Fig. 7(g) exhibits the size distribution of the crystalline precipitates from SANS data fitting. With UT time increases from 0 to 0.065 s, the sample demonstrates a visible scattered size distribution with the characteristic size decreases from 2.9 to 2.5 nm. As the further increase of UT times, the particle characteristic size increases to 5.7 nm. These results, in consistent with high-energy XRD measurements, indicate that the newly generated configurations resulting from UT have a different scattering density compared with the as-cast MG, which leads to the significantly structural heterogeneity of the sample during the UT process [99]. Furthermore, the FWHM of size distribution curves of the sample under UT at different times is shown in Fig. 7(h). It can be seen that the FWHM value increases from 5.38 to 6.74 nm with increasing UT times, suggesting the cluster inherited from the liquid structure distributes more extensively within the amorphous matrix. Our previous investigation on Fe-Si-B MG, such as $Fe_{78}Si_9B_{13}$ [100], has exhibited excellent degradation performances after UT, even without Cr. The $Fe_{76}Cr_2Si_{11}B_{11}$ MG, however, exhibits slightly smaller crystalline precipitate sizes and a much broader size distribution under UT as compared to Fe-Si-B MGs, especially at shorter durations, indicating higher structural stability, as depicted in Fig. S13.

To further investigate the evolution of structural order, detailed HRTEM analyses about atomic configurations are performed. Previously, it is reported that the structural evolution of Zr-based MGs can be revealed by analyzing their local atomic order that derives from the Fourier patterns based on the measured HRTEM images [57]. To quantitatively analyze the ordered structure of MGs before and after UT, the HRTEM images of 0, 1000, and 1250 J samples with scanning bars of 10 nm are measured, as shown in Fig. 7(i), (j), (k), respectively. The 2D ACF images of 0 and 1250 J samples are depicted in Fig. 7(l), (m), and (n), respectively, in which the ordered unit cell is highlighted by a yellow square. Therefore, the areal fraction of short-range order for 0, 1000, and 1250 J samples are determined to be 9%, 13%, and 21%, respectively. Obviously, the long-time UT results in a more ordered structure of MGs, coinciding with the aforementioned results.

3.4. UT-assistant degradation mechanism

In fact, the catalytic capability of MGs is fundamentally governed by their external morphology and internal atomic configurations. During the UT process, a collection of significant morphological characteristics appeared on amorphous powders. On the one hand, cold welding between particles induced by UT, analogous to observations in the previously reported $Zr_{55}Cu_{30}Al_{10}Ni_5$ MGs and amorphous SiO_2 glasses [48, 101], transforms isolated spherical particle into high-surface-area ellipsoids and dumbbells, accompanied by a 52.8% increase in average particle size, as illustrated in Fig. 1 (d). Meanwhile, these stress-induced surface cracking normally generates abundant percolation channels (see Fig. S1), which expose fresh amorphous phase with mass active sites under rapid mechanical stirring [102,103], and temporarily reverting the particle surface to a hydrophilic state that enhances solution-catalyst contact, eventually promoting the mass transport during degradation [100]. These morphological modulations collectively contribute to the 28-fold degradation efficiency in degradation efficiency for the 1250 J MG as compared to the 0 J MG, see Fig. 4(b).

It is accepted that MGs are thermodynamic instability with intrinsic structural heterogeneity [52], abundant inner flow units are regarded to be key for the high degradation ability [104]. Fig. 8 shows the schematic diagram of the degradation mechanism based on the evolution of defects and energy states during the ordering process induced by UT. From the potential energy landscape (PEL) perspective, the glassy system possesses a high Gibbs free energy and typically resides at a high energy position on the PEL diagram [50], thereby, the internal atomic rearrangement only needs to overcome a small energy barrier (ΔE_1), as shown in the top panel of Fig. 8. Because of the rapid cooling process, some clusters that inherit from liquid state were frozen due to the strong structural and dynamical heterogeneity in metalloid/non-metallic-containing systems [29], and meanwhile widely distributed within the amorphous matrix, as illustrated in the bottom panel of Fig. 8. With increasing UT time, these pre-existing clusters initiate annihilation and rearrangement as a result of the high-energy injection. Meanwhile, a high interatomic repulsion indicates a loose atomic packing state as the UT time increases to 1.029 s, see Fig. 2(d). From the SANS measurement in Fig. 7, the particle size distribution becomes broader (5.75 nm) compared to the as-cast MG (5.38 nm), accompanied by smaller characteristic crystalline particle sizes. It is attributed to the generation of some reconstructed clusters extensively distributed in the amorphous matrix, which leads to the MG sample exhibiting a high-energy excitation state. In this case, the atomic rearrangement only needs to overcome a smaller energy barrier (ΔE_2), which will contribute to the rapid

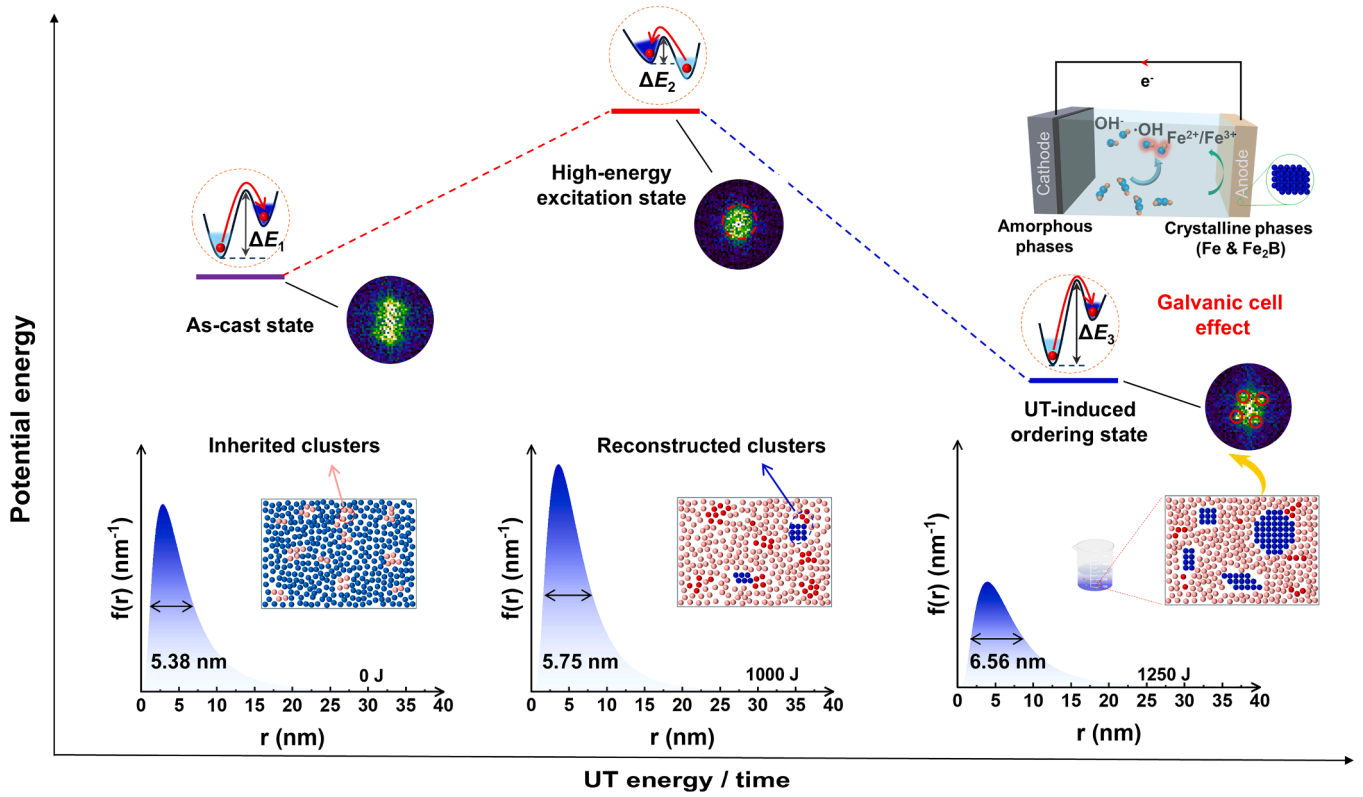

Fig. 8. Schematic diagram of UT-induced degradation mechanism from the defect and energy perspectives during the ordering process.

acceleration of degradation capability, like the previously reported Fe-based MG with a high-energy rejuvenation state [100].

The atomic configuration transitions from a disordered to a more ordered state with further increasing UT time, as confirmed by the decreased first peak width, remarkable Bragg peaks (Fig. 1(g)) and Fe/Fe_2B precipitation (Fig. 3(g)), forming a typical crystalline/amorphous composite. Besides, the notable improvements of SANS intensity, particle size distribution, and characteristic crystalline precipitates for the 1250 J sample indicate the distinct structural inhomogeneity. Some inherited clusters have been annihilated, while numerous newly formed large crystalline phases with a low-energy stable state (e.g., Fe and Fe_2B) have emerged. Consequently, the sample resides in a low position on the PEL diagram, like the state of nanocrystals induced by structural relaxation [105]. Simultaneously, such crystalline/amorphous composite structure may be beneficial for anti-corrosion, as depicted in Fig. 6(c). Interestingly, despite the increment of energy barrier (ΔE_3) due to the ordering processing, the degradation reactivity is not diminished, in fact, there is a significant improvement of the degradation ability with k of 0.751 min^{-1} in the 1250 J sample, which is 1.22 times higher than the 1000 J sample. The galvanic cell effect is recognized as an effective mechanism to enhance the rate of electron donation during the catalytic degradation process, which can be formed between the crystalline phase and the amorphous matrix due to their electrochemical potential difference [13]. Previously, the thermal treatment was employed to achieve the galvanic cell effect of MGs, such as $Fe_{75}P_{15}C_{10}$ and $Fe_{73.5}Si_{13.5}B_9Cu_1Nb_3$ MGs [44,104]. Generally, the Fe phase demonstrates lower electrochemical potential compared to other intermetallics, which facilitates the formation of nanoscale galvanic cells between Fe nanocrystals and other phases [13]. Nevertheless, the atomic rearrangement and free volume annihilation due to the thermal motion during the annealing process, accompanied by the gradual elimination of the residual stress, in turn are detrimental to the catalytic capability of MGs [104]. In our study, the galvanic cell effect is realized and amplified due to the potential difference of the coexisted nanocrystals and amorphous phases in the 1250 J sample after prolonged UT, in which the stable crystalline phase as anode exhibits low electrical resistivity and facilitates the transportation of electrons [106], while the metastable amorphous phase still exhibits a UT-induced high-energy state acts as excellent cathode for electron donation. Moreover, the direct energy injection by UT can retain residual stress while avoiding free volume annihilation common in annealing [107,108], giving rise to the generation of more active sites. Therefore, the UT-induced ordered state in MGs endows an exceptional degradation capability as compared with traditional postprocessing methods [44,106,108].

In fact, it has been reported that introducing crystalline phases into amorphous matrix can significantly improve properties of amorphous materials in some cases. For example, the $Fe_{80}Cu_4B_{14}P_2$ amorphous alloy with few nanocrystals illustrates high catalytic performance for wastewater purification, which is much better than fully amorphous and crystalline counterparts [42]. In addition, Meena and co-workers reported an active Ni_2P@$FePO_xH_y$ electrocatalyst that exhibits abundant interfaces between amorphous phosphorus-doped metal-oxide and crystalline metal phosphide, which provides rich electroactive sites and accelerates electron transfer, eventually contributing to a high current density (j) =1 A cm^{-2} at a low overpotential (η) = 360 mV in 1 M KOH with long-term durability of 12 days [109]. Sulaiman et al. also found that the active NiMoO/NF electrocatalyst with unique amorphous/crystalline structure can achieve the lowest overpotential of 115 mV at 100 mA cm^{-2} for the alkaline hydrogen evolution reaction [110]. Particularly, crystalline phase incorporation even effectively enhances the mechanical and magnetic properties of MGs. Liu et al. reported the $Fe_{26}Co_{25}Ni_{25}Al_3Ta_1Si_2B_{18}$ high-entropy MG with extraordinary soft magnetics and robust mechanics due to nanocrystal precipitations by annealing [111]. Evidently, appropriate incorporation of crystalline phases plays a crucial role in determining the mechanics, magnetism, and catalysis of amorphous materials, although their underlying mechanisms are dissimilar and some even still blur. Our work might provide a

novel UT-assisted nanocrystalline strategy for manipulating the microstructure and properties of amorphous materials. This approach not only offers new insights into the hybrid amorphous-crystalline material design but also opens avenues for developing advanced functional materials with tailored performance for applications in catalysis, energy conversion, and structural engineering.

4. Conclusion

In conclusion, this work demonstrates a breakthrough in degradation performances of MGs through UT-modulated structural order and surface welding, achieving an excellent degradation efficiency with an outperforming k of 0.751 min^{-1}, which surpasses conventional Fenton-like Fe-based MG catalysts by 50%. Our innovative strategy of precisely controlling UT unveils a novel activation mechanism.

MGs exhibit a rejuvenated high-energy excitation state at shorter UT processing times via liquid-like clusters reconstruction, as evidenced by the high interatomic repulsion and a wide particle size distribution, which reduces the energy barrier that the atomic rearrangement needs to overcome, thereby accelerating the azo dye degradation. With the UT time is prolonged, the amorphous configurations transform into a more pronounced ordered state compared to the as-cast state, characterized by the increased ordered fraction of 2D-ACFs by 2.3 fold and the characteristic particle size increases by 1.38 fold, which suggests more ordered clusters are formed due to UT, such as the growth of crystallized particles (i.e., Fe and Fe_2B phases). This process facilitates the formation of micro-galvanic cells between the metastable high-energy amorphous matrix and stable crystalline phases. Combined with the abundant active site channels due to the reconfiguration of surface morphology, these synergistic effects collectively enable exceptional degradation capability.

This work pioneers an advanced ultrasonic strategy for boosting the catalytic efficiency of MGs by precisely manipulating their structural order, offering transformative inspiration for designing next-generation catalysts for potential applications, including electrocatalysis, photocatalysis, energy storage, environmental remediation, biomedical engineering, etc., even establishing a fundamental theoretical framework for tailoring properties of amorphous materials through external fields.

CRediT authorship contribution statement

Wei Li: Writing – original draft, Investigation, Formal analysis, Data curation. **Jiayi Ruan:** Formal analysis, Data curation. **Zhenghao Gu:** Data curation. **Luyao Li:** Methodology, Data curation. **Hua Yang:** Methodology, Data curation. **Yubin Ke:** Data curation. **Xuelian Wu:** Methodology, Formal analysis. **Yujiao Lu:** Methodology. **Zheng Wang:** Methodology. **Fujun Lan:** Data curation. **Qiaoshi Zeng:** Resources. **Jiang Ma:** Resources. **Xun-Li Wang:** Writing – review & editing. **Chenchen Yuan:** Writing – review & editing, Supervision, Funding acquisition, Conceptualization.

Declaration of competing interest

The authors declare the following financial interests/personal relationships which may be considered as potential competing interests: The author Xun-Li Wang is an Editor for Acta Materialia and was not involved in the editorial review or the decision to publish this article.

Acknowledgments

This work was supported by the National Natural Science Foundation of China (Grant Nos. 52071078, 52401201), the Jiangsu Key Laboratory for Advanced Metallic Materials (Grant No. BM2007204), and the Big Data Computing Center of South University. Qiaoshi Zeng and Fujun Lan acknowledge the support from Shanghai Key Laboratory of Material Frontiers Research in Extreme Environments, China (No. 22dz2260800), the Shanghai Science and Technology Committee, China (No. 22JC1410300). Xun-Li Wang acknowledges the Croucher Foundation for the Croucher Senior Research Fellowship (CityU Project No. 9509008) and a grant at City University of Hong Kong (CityU Project No. 9229019).

Supplementary materials

Supplementary material associated with this article can be found, in the online version, at doi:10.1016/j.actamat.2025.121531.

References

[1] Z. Yao, Y. Chen, X. Wang, K. Hu, S. Ren, J. Zhang, Z. Song, N. Ren, X. Duan, High-entropy alloys catalyzing polymeric transformation of water pollutants with remarkably improved electron utilization efficiency, Nat. Commun. 16 (2025) 148.
[2] L.-C. Zhang, Z. Jia, F. Lyu, S.-X. Liang, J. Lu, A review of catalytic performance of metallic glasses in wastewater treatment: recent progress and prospects, Prog. Mater. Sci. 105 (2019) 100576.
[3] T. Robinson, G. McMullan, R. Marchant, P. Nigam, Remediation of dyes in textile effluent: a critical review on current treatment technologies with a proposed alternative, Bioresour. Technol. 77 (2001) 247–255.
[4] S. Xie, P. Huang, J.J. Kruzic, X. Zeng, H. Qian, A highly efficient degradation mechanism of methyl orange using Fe-based metallic glass powders, Sci. Rep. 6 (2016) 21947.
[5] M.T. Yagub, T.K. Sen, S. Afroze, H.M. Ang, Dye and its removal from aqueous solution by adsorption: a review, Adv. Colloid. Interface Sci. 209 (2014) 172–184.
[6] S.F. Ahmed, M. Mofijur, S. Nuzhat, A.T. Chowdhury, N. Rafa, M.A. Uddin, A. Inayat, T.M.I. Mahlia, H.C. Ong, W.Y. Chia, P.L. Show, Recent developments in physical, biological, chemical, and hybrid treatment techniques for removing emerging contaminants from wastewater, J. Hazard. Mater. 416 (2021) 125912.
[7] M.B. Ahmed, J.L. Zhou, H.H. Ngo, W. Guo, N.S. Thomaidis, J. Xu, Progress in the biological and chemical treatment technologies for emerging contaminant removal from wastewater: a critical review, J. Hazard. Mater. 323 (2017) 274–298.
[8] N.K. Amin, Removal of direct blue-106 dye from aqueous solution using new activated carbons developed from pomegranate peel: adsorption equilibrium and kinetics, J. Hazard. Mater. 165 (2009) 52–62.
[9] M. Punzi, A. Anbalagan, R. Aragão Börner, B.-M. Svensson, M. Jonstrup, B. Mattiasson, Degradation of a textile azo dye using biological treatment followed by photo-Fenton oxidation: evaluation of toxicity and microbial community structure, Chem. Eng. J. 270 (2015) 290–299.
[10] R. Patel, S. Suresh, Decolourization of azo dyes using magnesium–palladium system, J. Hazard. Mater. 137 (2006) 1729–1741.
[11] G.-I. Lupu, C. Orbeci, L. Bobirică, C. Bobirică, L.F. Pascu, Key principles of advanced oxidation processes: a systematic analysis of current and future perspectives of the removal of antibiotics from wastewater, Catalysts 13 (2023) 1280.
[12] Z. Jia, J.-L. Jiang, L. Sun, L.-C. Zhang, Q. Wang, S.-X. Liang, P. Qin, D.-F. Li, J. Lu, J.J. Kruzic, Role of boron in enhancing electron delocalization to improve catalytic activity of Fe-Based metallic glasses for persulfate-based advanced oxidation, ACS Appl. Mater. Interfaces. 12 (2020) 44789–44797.
[13] S. Chen, G. Yang, S. Luo, S. Yin, J. Jia, Z. Li, S. Gao, Y. Shao, K. Yao, Unexpected high performance of Fe-based nanocrystallized ribbons for azo dye decomposition, J. Mater. Chem. A 5 (2017) 14230–14240.
[14] Q. Wang, M. Chen, P. Lin, Z. Cui, C. Chu, B. Shen, Investigation of FePC amorphous alloys with self-renewing behaviour for highly efficient decolorization of methylene blue, J. Mater. Chem. A 6 (2018) 10686–10699.
[15] J. Hara, Oxidative degradation of benzene rings using iron sulfide activated by hydrogen peroxide/ozone, Chemosphere 189 (2017) 382–389.
[16] R. Broséus, S. Vincent, K. Aboulfadl, A. Daneshvar, S. Sauvé, B. Barbeau, M. Prévost, Ozone oxidation of pharmaceuticals, endocrine disruptors and pesticides during drinking water treatment, Water. Res. 43 (2009) 4707–4717.
[17] W. Zhao, C. Liang, B. Wang, S. Xing, Enhanced photocatalytic and Fenton-like performance of CuO_x-decorated $ZnFe_2O_4$, ACS Appl. Mater. Interfaces 9 (2017) 41927–41936.
[18] S.K. Bhunia, N.R. Jana, Reduced graphene oxide-silver nanoparticle composite as visible light photocatalyst for degradation of colorless endocrine disruptors, ACS Appl. Mater. Interfaces. 6 (2014) 20085–20092.
[19] J. Xu, Z. Wang, Y. Zhu, Enhanced visible-light-driven photocatalytic disinfection performance and organic pollutant degradation activity of porous g-C3N4 nanosheets, ACS Appl. Mater. Interfaces 9 (2017) 27727–27735.
[20] J. Guo, G. Song, X. Zhang, M. Zhou, Transition metal catalysts in the heterogeneous electro-Fenton process for organic wastewater treatment: a review, Environ. Sci-Wat. Res. Technol. 9 (2023) 2429–2445.
[21] A.D. Bokare, W. Choi, Review of iron-free Fenton-like systems for activating H_2O_2 in advanced oxidation processes, J. Hazard. Mater. 275 (2014) 121–135.
[22] W.H. Wang, C. Dong, C.H. Shek, Bulk metallic glasses, Mater. Sci. Eng. R. Rep. 44 (2004) 45–89.

[23] J. Li, I.-V. Soldatov, X.-C. Tang, B.-Y. Sun, R. Schäfer, S. Liu, Y.-Q. Yan, H.-B. Ke, Y. Sun, J. Orava, H. Bai, Metallic Mimosa pudica: a 3D biomimetic buckling structure made of metallic glasses, Sci. Adv. 8 (2022) eabm7658.

[24] S.Y. Liang, L.T. Zhang, Y.J. Wang, B. Wang, J.M. Pelletier, J.C. Qiao, A model on the coupling between cyclic fatigue and microstructure evolution in a metallic glass, Int. J. Fatigue 187 (2024) 108446.

[25] W. Li, C. Wang, L.Y. Li, C. Zhang, J. Ma, X.K. Xi, K. Tao, J.C. Qiao, C.C. Yuan, W. H. Wang, Manipulating defects in metallic glasses via ultrasonic treatment, Int. J. Mech. Sci. 287 (2025) 109960.

[26] L. Hou, B. Wang, L. Liu, X. Mao, M. Zhang, C. Yuan, Z. Li, W. Ju, H. Feng, C. Tang, A. Xia, W. Li, Tailoring magnetic softness of Fe-based amorphous alloys with superior magnetization by magnetic field annealing, J. Mater. Sci. Technol. 200 (2024) 27–37.

[27] D.-H. Kang, H. Zhang, H. Yoo, H.H. Lee, S. Lee, G.W. Lee, H. Lou, X. Wang, Q. Cao, D. Zhang, J. Jiang, Interfacial free energy controlling glass-forming ability of Cu-Zr Alloys, Sci. Rep. 4 (2014) 5167.

[28] Z. Jia, X. Duan, P. Qin, W. Zhang, W. Wang, C. Yang, H. Sun, S. Wang, L.-C. Zhang, Disordered atomic packing structure of metallic glass: toward ultrafast hydroxyl radicals production rate and strong electron transfer ability in catalytic performance, Adv. Funct. Mater. 27 (2017) 1702258.

[29] C.C. Yuan, F. Yang, F. Kargl, D. Holland-Moritz, M.Z. Li, X.L. Wang, B. Zhang, W. H. Wang, A. Meyer, Sluggish dynamics in Al-containing metallic glass-forming melts, Acta Mater. (2025) 285.

[30] L.C. Zhang, K.B. Kim, P. Yu, W.Y. Zhang, U. Kunz, J. Eckert, Amorphization in mechanically alloyed (Ti, Zr, Nb)–(Cu, Ni)–Al equiatomic alloys, J. Alloys. Compd. 428 (2007) 157–163.

[31] Y.C. Hu, Y.Z. Wang, R. Su, C.R. Cao, F. Li, C.W. Sun, Y. Yang, P.F. Guan, D. W. Ding, Z.L. Wang, W.H. Wang, A highly efficient and self-stabilizing metallic-glass catalyst for electrochemical hydrogen generation, Adv. Mater. 28 (2016) 10293–10297.

[32] F.-Y. Gao, S.-N. Liu, J.-C. Ge, X.-L. Zhang, L. Zhu, Y.-R. Zheng, Y. Duan, S. Qin, W. Dong, X. Yu, R.-C. Bao, P.-P. Yang, Z.-Z. Niu, Z.-G. Ding, W. Liu, S. Lan, M.-R. Gao, Y. Yan, S.-H. Yu, Nickel–molybdenum–niobium metallic glass for efficient hydrogen oxidation in hydroxide exchange membrane fuel cells, Nat. Catal. (2022).

[33] X. Chen, X.-J. Peng, D.-D. Xiao, Y.-T. Sun, K.-L. Zhou, X.-Y. Yang, Y.-Z. Zhang, W.-H. Wang, Z. Lu, H.-Y. Bai, High-efficiency electrochemical nitrogen fixation by noble-metal-free metallic glasses, Adv. Funct. Mater. (2025) e03400.

[34] J.-Q. Wang, Y.-H. Liu, M.-W. Chen, G.-Q. Xie, D.V. Louzguine-Luzgin, A. Inoue, J. H. Perepezko, Rapid degradation of azo dye by Fe-based metallic glass powder, Adv. Funct. Mater. 22 (2012) 2567–2570.

[35] Y. Tang, Y. Shao, N. Chen, K.-F. Yao, Rapid decomposition of direct blue 6 in neutral solution by Fe–B amorphous alloys, RSC Adv. 5 (2015) 6215–6221.

[36] C. Zhang, Z. Zhu, H. Zhang, Z. Hu, Rapid decolorization of acid Orange II aqueous solution by amorphous zero-valent iron, J. Environ. Sci. 24 (2012) 1021–1026.

[37] S.-X. Liang, X. Wang, W. Zhang, Y.-J. Liu, W. Wang, L.-C. Zhang, Selective laser melting manufactured porous Fe-based metallic glass matrix composite with remarkable catalytic activity and reusability, Appl. Mater. Today 19 (2020) 100543.

[38] H.X. Li, Z.C. Lu, S.L. Wang, Y. Wu, Z.P. Lu, Fe-based bulk metallic glasses: glass formation, fabrication, properties and applications, Prog. Mater. Sci. 103 (2019) 235–318.

[39] S. Wang, Y. Li, X. Wang, S. Yamaura, W. Zhang, Glass-forming ability, thermal properties, and corrosion resistance of Fe-based (Fe, Ni, Mo, Cr)-P-C-B metallic glasses, J. Non-Cryst. Solids 476 (2017) 75–80.

[40] S. Jiang, G. Cao, Z. Jia, L. Sun, C. Wang, H. Fan, Y. Wang, W. Xu, Y. Cui, Z. Ning, J. Sun, J. Li, X. Tang, H. Liang, E. Peng, A superb iron-based glassy-crystal alloy fiber as an ultrafast and stable catalyst for advanced oxidation, Adv. Fiber. Mater. 6 (2024) 1483–1494.

[41] Y.-H. Wang, B. Li, Y.-F. Cui, Y. Du, Z.-W. Yu, L.-Y. Zhang, Z.-L. Ning, X. Sun, J.-H. Li, X.-B. Tang, H. Liang, Q. Wang, P. E, J.-T. Huo, G. Wang, J.-F. Sun, S.-D. Jiang, Catalytic mechanism of nanocrystalline and amorphous matrix in Fe-based microwires for advanced oxidation, Adv. Funct. Mater. 35 (2025) 2425912.

[42] P. Zhang, Y.A. Zhu, Y. Zhang, T. Lu, Y. Pan, Heterogeneously structured FeCuBP amorphous–nanocrystalline alloy with excellent dye degradation efficiency, Appl. Phys. A 127 (2021) 330.

[43] Y. Zhao, Q. Chen, L. Ji, K. Wang, G. Huang, Strengthening mechanism of electrocatalytic properties of high activity Fe-based amorphous alloys by low escape work nanocrystals, J. Mater. Res. Technol. 29 (2024) 3135–3143.

[44] S.X. Liang, Z. Jia, Y.J. Liu, W. Zhang, W. Wang, J. Lu, L.C. Zhang, Compelling rejuvenated catalytic performance in metallic glasses, Adv. Mater. 30 (2018) e1802764.

[45] M. Liu, Y. Chen, J. Su, J. Shi, X. Wang, L. Guo, Photocatalytic hydrogen production using twinned nanocrystals and an unanchored NiS_x co-catalyst, Nat. Energy 1 (2016) 16151.

[46] J. Ma, C. Yang, X. Liu, B. Shang, Q. He, F. Li, T. Wang, D. Wei, X. Liang, X. Wu, Y. Wang, F. Gong, P. Guan, W. Wang, Y. Yang, Fast surface dynamics enabled cold joining of metallic glasses, Sci. Adv. 5 (2019) eaax7256.

[47] S. Sohrabi, J. Fu, L. Li, Y. Zhang, X. Li, F. Sun, J. Ma, W.H. Wang, Manufacturing of metallic glass components: processes, structures and properties, Prog. Mater. Sci. 144 (2024) 101283.

[48] L. Li, X. Li, Z. Huang, J. Huang, Z. Liu, J. Fu, W. Wen, Y. Zhang, S. Huang, S. Ren, J. Ma, Joining of metallic glasses in liquid via ultrasonic vibrations, Nat. Commun. 14 (2023) 6305.

[49] X. Li, D. Wei, J.Y. Zhang, X.D. Liu, Z. Li, T.Y. Wang, Q.F. He, Y.J. Wang, J. Ma, W. H. Wang, Y. Yang, Ultrasonic plasticity of metallic glass near room temperature, Appl. Mater. Today 21 (2020) 100866.

[50] P.G. Debenedetti, F.H. Stillinger, Supercooled liquids and the glass transition, Nature 410 (2001) 259–267.

[51] F.H. Stillinger, A Topographic view of supercooled liquids and glass formation, Science (1979) 267 (1995) 1935–1939.

[52] W.H. Wang, Dynamic relaxations and relaxation-property relationships in metallic glasses, Prog. Mater. Sci. 106 (2019) 100561.

[53] Y. Cheng, E. Ma, Atomic-level structure and structure–property relationship in metallic glasses, Prog. Mater. Sci. 56 (2011) 379–473.

[54] H. Luan, X. Zhang, H. Ding, F. Zhang, J.H. Luan, Z.B. Jiao, Y.C. Yang, H. Bu, R. Wang, J. Gu, C. Shao, Q. Yu, Y. Shao, Q. Zeng, N. Chen, C.T. Liu, K.F. Yao, High-entropy induced a glass-to-glass transition in a metallic glass, Nat. Commun. 13 (2022) 2183.

[55] F. Spieckermann, D. Şopu, V. Soprunyuk, M.B. Kerber, J. Bednarčík, A. Schökel, A. Rezvan, S. Ketov, B. Sarac, E. Schafler, J. Eckert, Structure-dynamics relationships in cryogenically deformed bulk metallic glass, Nat. Commun. 13 (2022) 127.

[56] Q. Wang, C.T. Liu, Y. Yang, J.B. Liu, Y.D. Dong, J. Lu, The atomic-scale mechanism for the enhanced glass-forming-ability of a Cu-Zr based bulk metallic glass with minor element additions, Sci. Rep. 4 (2014) 4648.

[57] Q. Wang, C.T. Liu, Y. Yang, Y.D. Dong, J. Lu, Atomic-scale structural evolution and stability of supercooled liquid of a Zr-based bulk metallic glass, Phys. Rev. Lett. 106 (2011) 215505.

[58] W. Li, X.F. Zuo, R. Liu, C.M. Pang, F. Jin, W.W. Zhu, C.C. Yuan, Multi-scale defects activation in $Gd_{18.33}Tb_{18.33}Dy_{18.34}Co_{17.5}Al_{27.5}$ high-entropy metallic glasses revealed by nanoindentation, Int. J. Plast. 174 (2024) 103893.

[59] F. Ning, W. Cong, Ultrasonic vibration-assisted (UV-A) manufacturing processes: state of the art and future perspectives, J. Manuf. Process. 51 (2020) 174–190.

[60] H. Lou, Z. Zeng, F. Zhang, S. Chen, P. Luo, X. Chen, Y. Ren, V.B. Prakapenka, C. Prescher, X. Zuo, T. Li, J. Wen, W.-H. Wang, H. Sheng, Q. Zeng, Two-way tuning of structural order in metallic glasses, Nat. Commun. 11 (2020) 314.

[61] C.C. Yuan, C. Deng, H.P. Zhang, M.Z. Li, B.L. Shen, Ab initio simulations of the atomic and electronic environment around B in Fe–Nb–B metallic glasses, Intermetallics (2019) 112.

[62] J. Krausser, K.H. Samwer, A. Zaccone, Interatomic repulsion softness directly controls the fragility of supercooled metallic melts, Proc. Natl. Acad. Sci. 112 (2015) 13762–13767.

[63] J. Yu, Z. Wang, L. Hu, W. Chu, Y. Bai, The anharmonicity role of interatomic potential in predicting glass formation, Scr. Mater. 216 (2022) 114737.

[64] Z. Wang, F. Yang, A. Bernasconi, K. Samwer, A. Meyer, Predicting structural and dynamical behavior of La-based glasses and melts from the anharmonicity in their interatomic potential, Phys. Rev. B 98 (2018) 024204.

[65] C.C. Yuan, Z.W. Lv, X. Li, C.M. Pang, R. Liu, C. Yang, J. Ma, W.W. Zhu, B. Huang, H.B. Ke, Ultrasonic-promoted defect activation and structural rejuvenation in a La-based metallic glass, Intermetallics 153 (2023) 107803.

[66] C. Yuan, R. Liu, Z. Lv, X. Li, C. Pang, C. Yang, J. Ma, W. Wang, Softening in an ultrasonic-vibrated Pd-based metallic glass, Intermetallics 144 (2022) 107527.

[67] C. Reichardt, Solvatochromic dyes as solvent polarity indicators, Chem. Rev. 94 (1994) 2319–2358.

[68] X. Qin, J. Xu, Z. Zhu, Z. Li, D. Fang, H. Fu, S. Zhang, H. Zhang, $Co_{78}Si_8B_{14}$ metallic glass: a highly efficient and ultra-sustainable Fenton-like catalyst in degrading wastewater under universal pH conditions, J. Mater. Sci. Technol. 113 (2022) 105–116.

[69] S.X. Liang, Z. Jia, W.C. Zhang, W.M. Wang, L.C. Zhang, Rapid malachite green degradation using $Fe_{73.5}Si_{13.5}B_9Cu_1Nb_3$ metallic glass for activation of persulfate under UV–Vis light, Mater. Des. 119 (2017) 244–253.

[70] L. Ji, J.W. Chen, Z.G. Zheng, Z.G. Qiu, S.Y. Peng, S.H. Zhou, D.C. Zeng, Excellent degradation performance of the $Fe_{78}Si_{11}B_9P_2$ metallic glass in azo dye treatment, J. Phys. Chem. Solids. 145 (2020) 109546.

[71] X.-F. Li, S.-X. Liang, X.-W. Xi, Z. Jia, S.-K. Xie, H.-C. Lin, J.-P. Hu, L.-C. Zhang, Excellent performance of $Fe_{78}Si_9B_{13}$ metallic glass for activating peroxymonosulfate in degradation of naphthol green B, Metals 7 (2017) 273.

[72] H. Sun, H. Zheng, X. Yang, Efficient degradation of orange II dye using Fe-based metallic glass powders prepared by commercial raw materials, Intermetallics 129 (2021) 107030.

[73] J. Wei, Z. Zheng, L. Zhao, Z. Qiu, D. Zeng, Synergistic effect between pyrite and Fe-based metallic glass for the removal of azo dyes in wastewater, Colloids Surfaces A 666 (2023) 131227.

[74] A. Lassoued, L.J. Liu, J.F. Li, Removal of acid orange II azo dyes using Fe-based metallic glass catalysts by Fenton-like process, J. Mater. Sci. 57 (2022) 2039–2052.

[75] S.-X. Liang, W. Zhang, L. Zhang, W. Wang, L.-C. Zhang, Remediation of industrial contaminated water with arsenic and nitrate by mass-produced Fe-based metallic glass: toward potential industrial applications, Sustain. Materi. Technol. 22 (2019) e00126.

[76] Z. Jia, J. Kang, W.C. Zhang, W.M. Wang, C. Yang, H. Sun, D. Habibi, L.C. Zhang, Surface aging behaviour of Fe-based amorphous alloys as catalysts during heterogeneous photo Fenton-like process for water treatment, Appl. Catal. B: Environ. 204 (2017) 537–547.

[77] Z. Jia, X. Duan, W. Zhang, W. Wang, H. Sun, S. Wang, L.C. Zhang, Ultra-sustainable Fe78Si9B13 metallic glass as a catalyst for activation of persulfate on methylene blue degradation under UV-Vis light, Sci. Rep. 6 (2016) 38520.

[78] Y. Tang, Y. Shao, N. Chen, X. Liu, S.Q. Chen, K.F. Yao, Insight into the high reactivity of commercial Fe–Si–B amorphous zero-valent iron in degrading azo dye solutions, RSC Adv. 5 (2015) 34032–34039.
[79] X. Qin, Z. Li, Z. Zhu, H. Fu, H. Li, A. Wang, H. Zhang, H. Zhang, Mechanism and kinetics of treatment of acid orange II by aged Fe-Si-B metallic glass powders, J. Mater. Sci. Technol. 33 (2017) 1147–1152.
[80] P. Liu, J.L. Zhang, M.Q. Zha, C.H. Shek, Synthesis of an Fe rich amorphous structure with a catalytic effect to rapidly decolorize azo dye at room temperature, ACS Appl. Mater. Interfaces. 6 (2014) 5500–5505.
[81] H.-L. Li, Z.-W. Zhu, S. Li, S. Bao, C.-M. Liu, S. Zhang, H.-f. Zhang, Degradation mechanism of acid orange II in persulfate/Fe-based metallic glass system, J. Phys. Chem. Solids. 160 (2022) 110316.
[82] C. Zhang, Z. Zhu, H. Zhang, Z. Hu, Rapid reductive degradation of azo dyes by a unique structure of amorphous alloys, Chin. Sci. Bull. 56 (2011) 3988–3992.
[83] S.-H. Xie, G.-Q. Peng, X.-M. Tu, H.-X. Qian, X.-R. Zeng, Fe-based powders prepared by ball-milling with considerable degradation efficiency to methyl orange compared with Fe-based metallic glasses, Acta Metall. Sin. 31 (2018) 1207–1214.
[84] S.-Q. Chen, M. Li, X.-Y. Ma, M.-J. Zhou, D. Wang, M.-Y. Yan, Z. Li, K.-F. Yao, Influence of inorganic ions on degradation capability of Fe-based metallic glass towards dyeing wastewater remediation, Chemosphere 264 (2021) 128392.
[85] N. Weng, F. Wang, F. Qin, W. Tang, Z. Dan, Enhanced azo-dyes degradation performance of Fe-Si-B-P nanoporous architecture, Materials 10 (2017) 1001.
[86] C. Zhang, H. Zhang, M. Lv, Z. Hu, Decolorization of azo dye solution by Fe–Mo–Si–B amorphous alloy, J. Non-Cryst. Solids 356 (2010) 1703–1706.
[87] C. Zhang, Z. Zhu, H. Zhang, Z. Hu, On the decolorization property of Fe–Mo–Si–B alloys with different structures, J. Non-Cryst. Solids 358 (2012) 61–64.
[88] C. Zhang, Q. Sun, Annealing-induced different decolorization performances of Fe-Mo-Si-B amorphous alloys, J. Non-Cryst. Solids 470 (2017) 93–98.
[89] C. Zhang, Z. Zhu, H. Zhang, Effects of the addition of Co, Ni or Cr on the decolorization properties of Fe-Si-B amorphous alloys, J. Phys. Chem. Solids 110 (2017) 152–160.
[90] S.-X. Liang, W. Zhang, W. Wang, G. Jia, W. Yang, L.-C. Zhang, Surface reactivation of FeNiPC metallic glass: a strategy for highly enhanced catalytic behavior, J. Phys. Chem. Solids 132 (2019) 89–98.
[91] L. Hou, Q. Wang, X. Fan, F. Miao, W. Yang, B. Shen, Effect of Co addition on catalytic activity of FePCCu amorphous alloy for methylene blue degradation, New. J. Chem. 43 (2019) 6126–6135.
[92] Z. Jia, S.X. Liang, W.C. Zhang, W.M. Wang, C. Yang, L.C. Zhang, Heterogeneous photo Fenton-like degradation of cibacron brilliant red 3B-A dye using amorphous $Fe_{78}Si_9B_{13}$ and $Fe_{73.5}Si_{13.5}B_9Cu_1Nb_3$ alloys: the influence of adsorption, J. Taiwan. Inst. Chem. Eng. 71 (2017) 128–136.
[93] S. Chen, N. Chen, M. Cheng, S. Luo, Y. Shao, K. Yao, Multi-phase nanocrystallization induced fast degradation of methyl orange by annealing Fe-based amorphous ribbons, Intermetallics 90 (2017) 30–35.
[94] S. Chen, M. Li, Q. Ji, T. Feng, S. Lan, K. Yao, Effect of the chloride ion on advanced oxidation processes catalyzed by Fe-based metallic glass for wastewater treatment, J. Mater. Sci. Technol. 117 (2022) 49–58.
[95] E. Pekarskaya, J.F. Löffler, W.L. Johnson, Microstructural studies of crystallization of a Zr-based bulk metallic glass, Acta Mater. 51 (2003) 4045–4057.
[96] L. Yang, M.K. Miller, X.-L. Wang, C.T. Liu, A.D. Stoica, D. Ma, J. Almer, D. Shi, Nanoscale solute partitioning in bulk metallic glasses, Adv. Mater. 21 (2009) 305–308.
[97] S. Lan, Y. Ren, X.Y. Wei, B. Wang, E.P. Gilbert, T. Shibayama, S. Watanabe, M. Ohnuma, X.L. Wang, Hidden amorphous phase and reentrant supercooled liquid in Pd-Ni-P metallic glasses, Nat. Commun. 8 (2017) 14679.
[98] X. Wu, S. Lan, X. Li, M. Yang, Z. Wu, X. Wei, H. He, M. Naeem, J. Zhou, Z. Lu, E. P. Gilbert, D. Ma, X.-L. Wang, Continuous chemical redistribution following amorphous-to-crystalline structural ordering in a Zr-Cu-Al bulk metallic glass, J. Mater. Sci. Technol. 101 (2022) 285–293.
[99] Y. Cao, M. Yang, Q. Du, F.-K. Chiang, Y. Zhang, S.-W. Chen, Y. Ke, H. Lou, F. Zhang, Y. Wu, H. Wang, S. Jiang, X. Zhang, Q. Zeng, X. Liu, Z. Lu, Continuous polyamorphic transition in high-entropy metallic glass, Nat. Commun. 15 (2024) 6702.
[100] Z. Lv, Y. Yan, C. Yuan, B. Huang, C. Yang, J. Ma, J. Wang, L. Huo, Z. Cui, X. Wang, W. Wang, B. Shen, Making Fe-Si-B amorphous powders as an effective catalyst for dye degradation by high-energy ultrasonic vibration, Mater. Des. 194 (2020) 108876.
[101] Y. Guo, H. Cui, P. Jia, Z. Ye, L. Deng, H. Li, B. Guo, X. Zhang, J. Huang, Y. Su, J. Huang, B. Wen, Y. Lu, L. Zhang, Nanoscale cold welding of glass, Matter (2024) 4390–4397.
[102] Q. Wang, L. Yun, M. Chen, D. Xu, Z. Cui, Q. Zeng, P. Lin, C. Chu, B. Shen, Competitive effects of structural heterogeneity and surface chemical states on catalytic efficiency of FeSiBPCu amorphous and nanocrystalline alloys, ACS Appl. Nano Mater. 2 (2019) 214–227.
[103] Z. Zeng, N. Liu, Q. Zeng, S.W. Lee, W.L. Mao, Y. Cui, In situ measurement of lithiation-induced stress in silicon nanoparticles using micro-Raman spectroscopy, Nano Energy 22 (2016) 105–110.
[104] Q. Chen, Z. Qi, Y. Feng, H. Liu, Z. Wang, L. Zhang, W. Wang, Nanostructured metallic glass contributing to efficient catalytic degradation of dye wastewater, J. Non-Cryst. Solids 598 (2022) 121952.
[105] H. Zhao, F. Sun, X. Li, Y. Ding, Y.Q. Yan, X. Tong, J. Ma, H.B. Ke, W.H. Wang, Ultrastability of metallic supercooled liquid induced by vibration, Scr. Mater. 194 (2021) 113606.
[106] X. Peng, J. Han, Y. Wang, Z. Bo, A. Nie, P. Li, Y. Li, H. Wu, P. Liu, Z. Lu, H. Bai, Unexpected enhanced catalytic performance via highly dense interfaces in ultra-fine amorphous-nanocrystalline biphasic structure, Appl. Mater. Today 29 (2022) 101689.
[107] C. Ma, H. Qin, Z. Ren, S.C. O'Keeffe, J. Stevick, G.L. Doll, Y. Dong, B. Winiarski, C. Ye, Increasing fracture strength in bulk metallic glasses using ultrasonic nanocrystal surface modification, J. Alloys. Compd. 718 (2017) 246–253.
[108] S.-Q. Chen, Y. Shao, M.-T. Cheng, K.-F. Yao, Effect of residual stress on azo dye degradation capability of Fe-based metallic glass, J. Non-Cryst. Solids 473 (2017) 74–78.
[109] A. Meena, P. Thangavel, D.S. Jeong, A.N. Singh, A. Jana, H. Im, D.A. Nguyen, K. S. Kim, Crystalline-amorphous interface of mesoporous Ni_2P @ $FePO_xH_y$ for oxygen evolution at high current density in alkaline-anion-exchange-membrane water-electrolyzer, Appl. Catal. B Environ. 306 (2022) 121127.
[110] R.R. Binti Raja Sulaiman, K.S. Loh, R.M. Yunus, A. Hanan, M. Khalid, T.F. Choo, Y. Tao, J. Shao, W.Y. Wong, Phase transition and electrocatalytic properties of a 1-dimensional NiMo amorphous-crystalline alloy for the alkaline hydrogen evolution reaction, Int. J. Hydro. Energy 92 (2024) 865–876.
[111] L. Liu, L. Shao, Y. Ma, Z. Wen, J. Zhou, Y. Yan, W. Yang, H. Ke, W. Wang, Sparse nanocrystals enable ultra-low coercivity and remarkable mechanical robustness in high-entropy amorphous alloy, Adv. Sci. (2025) e03546.